

Contents

2	1 Introduction	3
3	2 Pixel detectors	5
4	2.1 Signal formation	5
5	2.2 Charge Coupled Devices	7
6	2.3 Hybrid pixels	7
7	2.4 CMOS MAPS and DMPAS	9
8	2.4.1 DMAPS: large and small fill factor	10
9	2.4.2 A modified sensor	11
10	2.5 Analog front end	13
11	2.5.1 Preamplifier	13
12	2.6 Readout logic	14
13	3 Use of pixel detectors	17
14	3.1 Tracking in HEP	17
15	3.1.1 Hybrid pixels at LHC and at SuperKEKB	18
16	3.1.2 First attempts to MAPS	20
17	3.2 Other applications	23
18	3.2.1 Applicability to FLASH radiotherapy	23
19	4 TJ-Monopix1	28
20	4.1 The sensor	29
21	4.2 Front end	31
22	4.2.1 ALPIDE-like	32
23	4.3 Readout logic	33
24	5 Arcadia-MD1	37
25	5.1 The sensor	37
26	5.2 Readout logic and data structure	38
27	5.2.1 Matrix division and data-packets	38
28	6 Characterization	41
29	6.1 TJ-Monopix1 characterization	41
30	6.1.1 Threshold and noise: figure of merit for pixel detectors	41
31	6.1.2 Linearity of the ToT	44
32	6.1.3 Calibration of the ToT	46
33	6.1.4 PMOS flavor: changing the bias	49
34	6.1.5 Measurements with radioactive sources	50

35	6.1.6	Dead time measurements	52
36	6.2	ARCADIA-MD1 characterization	54
37	7	Test beam measurements	55
38	7.1	Apparatus description	55
39	7.1.1	Accelerator	56
40	7.1.2	Mechanical carriers	57
41	7.2	Measurements	57
42	7.2.1	MIP spectrum using cosmic rays as source	62
43	A	Pixels detector: a brief overview	63
44	A.1	Radiation damages	63
45	Bibliography		66
46	Characterization of monolithic CMOS pixel sensors for charged particle detectors and		
47	for high intensity dosimetry		

⁴⁸

Chapter 1

⁴⁹

Introduction

⁵⁰ Since the 1980s, when the fabrication of device with very small electrodes (50-100 μm)
⁵¹ became a practical possibility, pixel detectors have been widely employed for imaging and
⁵² tracking charged particles in the vertex region of experiments at accelerators. Thanks
⁵³ to their excellent spatial resolution, today even better than 10 μm , they allow for true
⁵⁴ three-dimensional space-point determination even at high particle fluxes and in particular
⁵⁵ for the identification of secondary vertices of short-lived particles such as τ and B mesons.
⁵⁶ Requirement imposed by accelerator are stringent and they will become even more with the
⁵⁷ increase of luminosity; in this scenario CMOS Monolithic Active Pixel Sensors (MAPS) are
⁵⁸ being developed to improve the performance of the hybrid pixel detectors, which currently
⁵⁹ constitute the state-of-art for large scale pixel detector, in particular by reducing the
⁶⁰ amount of material, power consumption and pixel dimension.

⁶¹ Experiments such as ALICE at LHC and STAR at RHIC have already introduced the
⁶² CMOS MAPS technology in their detectors. ALICE Tracking System (ITS2), upgraded
⁶³ during the LHC long shut down in 2019-20, was the first large-area ($\sim 10 \text{ m}^2$) silicon vertex
⁶⁴ detector based on CMOS MAPS. Thanks to the reduction of the material budget, ITS2,
⁶⁵ which uses the ALPIDE chip developed by ALICE collaboration, obtained an amazing im-
⁶⁶ provement both in the position measurement and in the momentum resolution, improving
⁶⁷ the efficiency of track reconstruction for particle with very low transverse momentum (by
⁶⁸ a factor 6 at $p_T \sim 0.1 \text{ GeV}/c$). Further advancements in CMOS MAPS technology are
⁶⁹ being aggressively pursued for the ALICE ITS3 and the Belle II vertex detector upgrades
⁷⁰ (both foreseen around 2026-27) and by the R&D53 collaboration for the upgrade at HL-
⁷¹ LHC, with the goals of further reducing the sensor thickness and improving the readout
⁷² speed of the devices, while keeping power consumption at a minimum.

⁷³ Beside tracking, the development of pixel detectors is a very active field with many
⁷⁴ applications: a noteworthy example of detector originally used in particle physics, and
⁷⁵ later employed mainly for medical imaging, but also in space and for art authentication, is
⁷⁶ Medipix, a hybrid system developed at CERN within the Medipix collaboration. Among
⁷⁷ medical applications, a possible use of CMOS MAPS could be in dosimetry: in the last few
⁷⁸ years the search of radiotherapy oncological treatments with high intensity beams (FLASH
⁷⁹ mode) is requiring new dosimeters, both for the therapies as well as new beam-monitors
⁸⁰ (especially for focused very high energy electron beams), which are capable of deal with
⁸¹ extreme dose rate (up to 40 Gy/s).

⁸² I've studied the characteristics of two ALPIDE-like CMOS MAPS chips and tested
⁸³ them under different front end configuration. The first chip, the TJ-Monopix1 from the

84 Monopix series, is a TowerJazz MAPS fabricated in 180 nm CMOS technology and is one
85 of the prototypes for the Belle II vertex detector upgrade. The second chip, called Main
86 Demonstrator-1, is produced by LFoundry in 110 nm CMOS technology and designed by
87 the ARCADIA (Advanced Readout CMOS Architectures with Depleted Integrated sensor
88 Arrays) group; it is intended to be a general purpose device with possible use in medical
89 scanners, space experiments, future lepton colliders and also possibly X-ray applications
90 with thick substrates. The main differences between the two chips are in the output signal
91 type and in the readout sequence of the matrix. Concerning the former point TJ-Monopix1
92 returns an analog output information, that is the time over threshold of the pulse which
93 can be related with the charge released by the particle in the sensor, while MD1 returns
94 only a digital information; regarding the latter, instead, TJ-Monopix1 has a completely
95 sequential readout, while MD1 grossly combines the information of the hits before the
96 readout in order to reduce the data transmission time.

97 I have set up two test systems for the two chips in the INFN clean laboratories and
98 characterized the devices electrically and with radioactive sources. In particular I have
99 performed the characterization of the chips to find the threshold and noise of the pixels
100 and their dispersion across the matrix, to have an absolute value in electrons of the signal
101 recorded by TJ-Monopix1, I've also performed an absolute calibration using a Fe55 x-ray
102 source and studied the dead time and the readout properties. Moreover, I've also test
103 TJ-Monopix1 at high dose rate with the FLASH-accelerator recently installed at Santa
104 Chiara hospital in Pisa, and I have participated in the design of the setup needed for test
105 beam measurement.

¹⁰⁶ **Chapter 2**

¹⁰⁷ **Pixel detectors**

¹⁰⁸ Pixel detectors are semiconductor detectors which are segmented in two dimensions: this
¹⁰⁹ distinguish them from the strip detectors, such that a single plane of detector already
¹¹⁰ provides both the coordinates of impact of the detected particle. Their operation is based
¹¹¹ on the p-n junction (fig. 2.1). A p-n junction is built by bringing in contact two n
¹¹² and p doped silicon crystals. At the boundary, recombination of both charge carriers
¹¹³ occurs forming a region, the depletion zone, which is free of charge carriers. The charged
¹¹⁴ donors⁺ and acceptor⁻, that remain ionised in the n-type and p-type regions, features a
¹¹⁵ space charge and create an electric field across the junction, causing a drift current in the
¹¹⁶ opposite direction to the diffusion one, through which the junction reaches an equilibrium
¹¹⁷ state. Assuming a constant space change, the electric field is linear and reach a maximum
¹¹⁸ at the boundary of the *p* and *n* layers.

¹¹⁹ **2.1 Signal formation**

¹²⁰ When a charged particle passes through a pixel and loses energy by ionization only a
¹²¹ part of that energy is used to generate electron-hole pairs, since another part is used for
¹²² other processes, as lattice excitation. The average energy needed to create a pair at 300 K
¹²³ in silicon is $w_i = 3.65 \text{ eV}$, that is more than the mean ionization energy because of the
¹²⁴ interactions with phonon, since for a minimum ionizing particle (MIP) the most probable
¹²⁵ value (MPV) of charge released in the semiconductor is $0.28 \text{ keV}/\mu\text{m}$, hence the number
¹²⁶ of electrons-vacuum pairs is:

$$\langle \frac{dE}{dx} \rangle \frac{1}{w_i} \sim 80 \text{ e/h} \sim \frac{1.28 \cdot 10^{-2} fC}{\mu\text{m}} \quad (2.1)$$

¹²⁷ Because of the splitting of the energy depositon between the two different processes, the
¹²⁸ number $N_{e/h}$ of couples generated undergoes fluctuations that usually follow a Poisson
¹²⁹ distribution; thus the fluctuations of $N_{e/h}$ is equal to $\sigma_{e/h} = \sqrt{N_{e/h}}$. Under the constraint
¹³⁰ of complete absorption of a particle, the energy resolution improves of a factor \sqrt{F} , where
¹³¹ F is called the Fano factor and determines the ultimate limit of energy resolution for
¹³² semiconductors. F is a function of the material and temperature and for silicon is equal
¹³³ to ~ 0.115 .

¹³⁴ In order to avoid a loss signal, it is fundamental that pairs e/h are produced in the
¹³⁵ depleted region of the semiconductor, where the probability of recombination with charge
¹³⁶ carriers is low. For this reason pixel detectors are commonly reverse biased: a positive
¹³⁷ bias is given to the *n* electrode and a negative to the *p* in order to grow the depletion zone

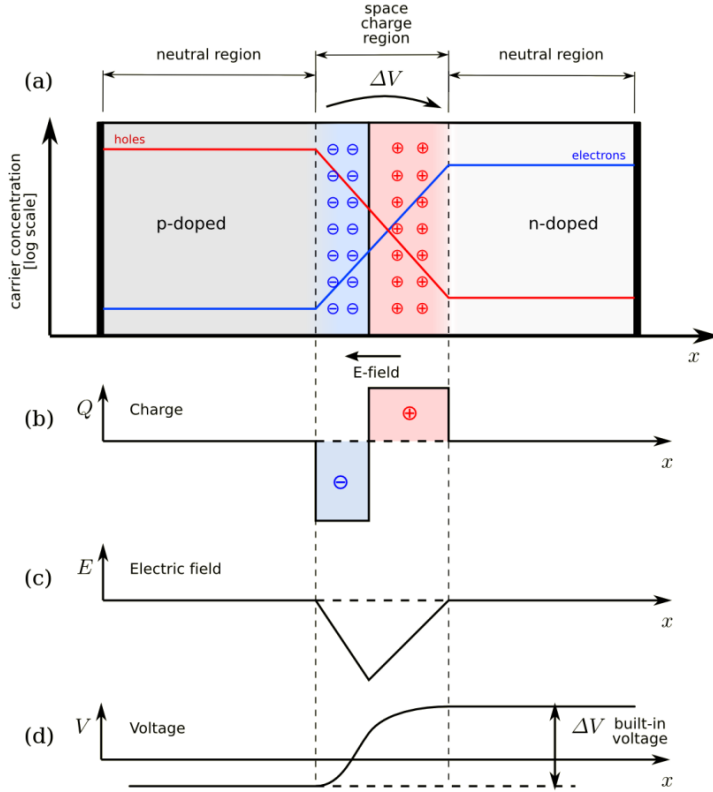


Figure 2.1: The structure of a p-n junction. (a) structure, (b) space charge density, (c) electric field distribution and (d) potential distribution.

in the epitaxial layer within the bulk. The width of the depletion region depends on the external bias V_{ext} , the resistivity ρ and also with the dopant:

$$d_n \sim 0.55 \sqrt{\frac{\rho}{\Omega cm} \frac{V_{ext}}{V}} \mu m \quad d_p \sim 0.32 \sqrt{\frac{\rho}{\Omega cm} \frac{V_{ext}}{V}} \mu m \quad (2.2)$$

Thus, high resistivity wafers ($100 \Omega cm - k\Omega cm$) are typically preferred because they allow bigger depletion zone with smaller voltage bias.

The charges created within the sensor are separated by an electric field and collected at their respective electrodes (p for holes and n for electrons)¹; by the drift of these charges, a signal i_e is generated on the electrode e as stated by the Shockley-Ramo's theorem:

$$i_e(t) = -q v(t) E_{WF,e} \quad (2.3)$$

where $v(t)$ is the instantaneous velocity of the charge q and E_{WF} is the weighting field, that is the field obtained biasing the electrode e with 1V and all the others with 0V. The drift velocity of the charge depends on the electric field and on the mobility of the particle:

$$v = \mu(E) E \quad (2.4)$$

where $\mu(E)$ is a function of the electric field and is linear in E only for small E : at higher values the probability of interactions with optical phonons increases, the mobility drops

¹Even if in principle both the electrode can be used to read the signal, for pixel detectors, where the number of channel and the complexity of readout are high, only one is actually used. In strip and pad detectors, instead, is more common a dual-side readout

150 and this leads to a saturation of the velocity (fig. 2.2). Typical values for electrons and
 151 holes mobility in silicon at room temperature are $\mu_n \sim 1450 \text{ cm}^2/\text{Vs}$, $\mu_h = 500$.

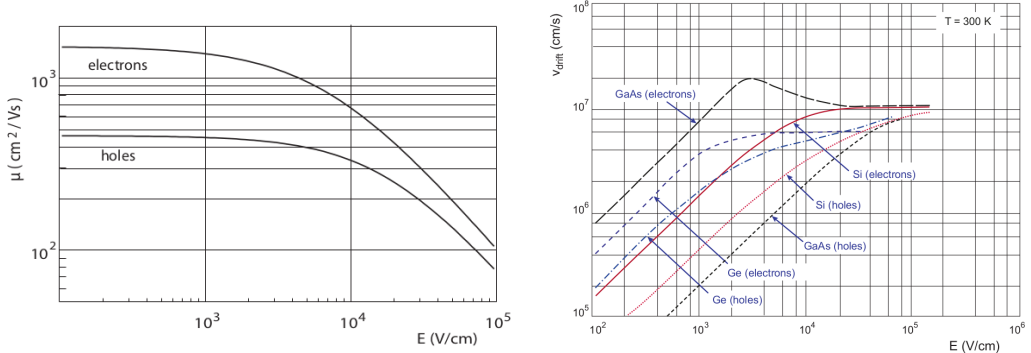


Figure 2.2: (a) Dependence of the mobility on the electric field. (b) Drift velocity at room temperature in different semiconductors

152 2.2 Charge Coupled Devices

153 In CCDs the charge is created in a very thin active epitaxial layer (typically 10 μm ,
 154 maximally about 30 μm) and then locally stored in a potential minimum which is created
 155 by a MOS structure. The size of the CCD cells is typically in the range 10 μm to 20 μm
 156 such that spatial resolutions are of the order of a few micrometres. The collected charges
 157 are moved stepwise from electrode to electrode (thus so called 'bucket chain') by applying a
 158 potential with a clock with frequency of \sim MHz; despite of such high frequency, the readout
 159 chain is completely sequential and this makes the entire process comparatively slow (tens
 160 of ms). A particular type of CCD, the pnCCDs, are typically used to detect low energy
 161 (<10 keV) x-ray photons for their homogeneous spatial detection efficiency of photons.
 162 The pnCCDs have a sideward depletion similar to silicon drift chambers that makes the
 163 electric field stronger, compared with the normal CCDs. The pnCCDs designed for photon
 164 imaging are often fabricated with high Z materials, to increase absorption efficacy.

165 2.3 Hybrid pixels

166 Hybrid pixels, which currently are the state-of-art technology for large scale pixel detectors
 167 in most particle physics experiments, are made of two parts welded together through
 168 microconnection (bump bond): the sensor and the electronics (fig. 2.3a). They provide a
 169 practical system where the sensor and the ASIC (application specific integrated circuit)
 170 can be optimized separately, which makes them really fast, capable of handling with rate
 171 up to GHz. However a disadvantage of hybrid pixels is that they must be connected before
 172 testing. For reasons related with the historical development, the n⁺-in-n sensors were the
 173 first to be used; they demanded double-sided processing which guarantees the detector
 174 functionality both before and after the type inversion of the n⁻ doped bulk into p-type
 175 after high quantity of radiation. The pn-diode is initially on the unstructured backside
 176 of the sensor, while after, the depletion zone grows from the electrode side into the bulk.
 177 This ensures that the signal can be sensed on the pixels even if the substrate is no longer
 178 fully depleted, even though the bias voltage required for a sufficient depletion increases,

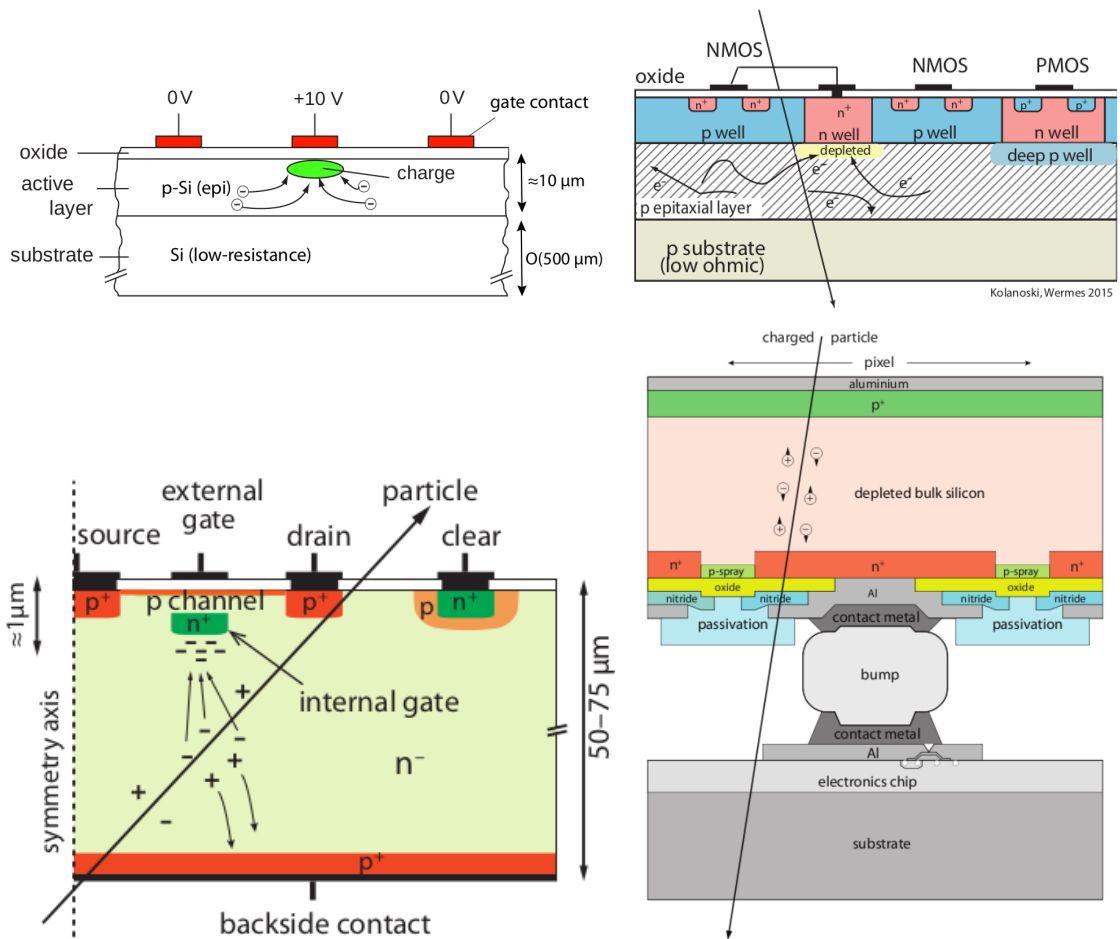


Figure 2.3: Concept cross-section of hybrid pixel (a) and of a DEPFET (b)

179 liming the detector lifetime up to a few years. With the availability of high quality p-
180 substrate material ($\gtrsim 2 \text{ k}\Omega\text{cm}$) the fabrication of n-in-p type sensors, which does not invert
181 anymore, became the preferred choise leading also a huge advance in cost reduction due
182 to no more need of double sided. However, the particular and sophisticated procedure to
183 bond sensor and ASIC makes them difficult to produce, delicate (especially when exposed
184 to high levels of radiation) and also expensive.

185 DEPFET are the first attempt towards the integration of the front end (FE) on the
186 sensor bulk: they are typically mounted on a hybrid structure but the sensor also in-
187 tegrates the first amplification stage. Each pixel implements a MOSFET (metal-oxide-
188 semiconductor field-effect transistor) transistor (a p-channel in fig. 2.3b): a hole current
189 flows from source to drain which is controlled by the external gate and the internal gate
190 together. The internal gate is made by a deep $n+$ implant towards which electrons drift
191 after being created in the depletion region; the accumulation of electrons in the region
192 underneath the n implant changes the gate potential and controls the transistor current.
193 DEPFET typically have a good S/N ratio: this is principally due to the amplification
194 on-pixel and to the large depletion region. But, as they need to be connected to an ASIC,
195 their limiting factor is still the material budget.

196 2.4 CMOS MAPS and DMPAS

197 Monolithic active pixels accommodate on the same wafer both the sensor and the FE
198 electronics, with the second one implanted on top within a depth of about $1 \mu\text{m}$ below
199 the surface. MAPS have been first proposed and realized in the 1990s and their practical
200 usage has been enabled by the development of the electronic sector, which guarantees the
201 halving of CMOS transistors dimension at least every two years, as stated by the Moore's
202 law. As a matter of fact the dimension of components, their organization on the pixel
203 area and logic density are important issues for the design and for the layout. Compared
204 to CCDs, the readout time is dramatically reduced by the in-pixel amplification and
205 discrimination, typically followed by a sparsified readout not requiring the signal to be
206 transported anymore over thousands of pixels; as aside effect, the radiation tolerance is
207 also greatly increased by sensing the signal charge directly within its own pixel.

208 A critical parameter for accelerator experiments is the material budget, which repre-
209 sents the main limit factor for momentum measurement resolution in a magnetic field;
210 since hybrid pixels are thicker (\sim hundreds of μm) than monolithic ones (even less than
211 $100 \mu\text{m}$). Using the latter the material budget can be down by a third: typical values for
212 hybrid pixels is $1.5 \% X_0$ per layer, while for monolithic $0.5 \% X_0$. Compared to MAPS,
213 among other disadvantages of hybrid pixels there is the bigger power consumption, that
214 requires also a bigger cooling system, leading to a futher increase of material.

215 Monolithic active pixel can be distinguished between two main categories: MAPS and
216 depleted MAPS (DMPAS). MAPS (figure a ??) have typically an epitaxial layer in a from
217 range $1 \mu\text{m}$ to $20 \mu\text{m}$ and, since they are not depleted, the charge is mainly collected by
218 diffusion rather than by drift. This makes the path of charges created in the bulk longer
219 than usual, making them slow (of order of 100 ns). Moreover, the collection can be partial,
220 especially after irradiation of the detector (look at A for radiation damages), when the
221 trapping probability becomes higher. In figure ?? it is shown as example of CMOS MAPS:
222 the sensor implements an n well as collection diode; to prevent the others n wells (which
223 contain PMOS transistor) of the electronic circuit competing in charge collection and to

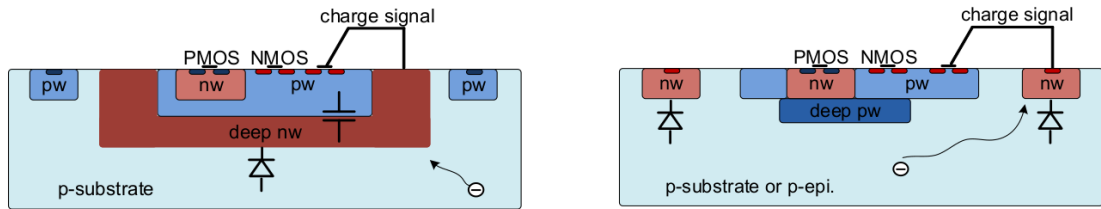


Figure 2.4: Concept cross-section with large and small fill factor

shield the CMOS circuit from the substrate, additional underlying deep p well are needed. DMAPS are instead MAPS depleted with d typically in $\sim 25 \mu\text{m}$ to $150 \mu\text{m}$ (eq. 2.2) which extends from the diode to the deep p-well, and sometimes also to the backside (in this case if one wants to collect the signal also on this electrode, additional process must be done).

2.4.1 DMAPS: large and small fill factor

There are two different sensor-design approaches (figure 2.4) to DMAPS:

- large fill factor: a large collection electrode that is a large deep n-well and that host the embedded electronics
- small fill factor: a small n-well is used as charge collection node

To implement a uniform and stronger electric field, DMAPS often uses large electrode design that requires multiple wells (typically four including deep n and p wells); with this layout the total capacity of the sensor increases because of the addition of a new term (fig. 2.5), which contributes to the total amplifier input capacity ($\sim 100 \text{ fF}$). In addition to the capacity between pixels (C_{pp}) and between the pixel and the backside (C_b), a non-negligible contribution comes from the capacities between wells (C_{SW} and C_{WW}) needed to shield the embedded electronics. These capacities affect the thermal and $1/f$ noise of the charge amplifier and the τ_{CSA} too:

$$ENC_{thermal}^2 \propto \frac{4}{3} \frac{kT}{g_m \tau_{sh}} \frac{C_D^2}{C_f} \quad \tau_{CSA} \propto \frac{1}{g_m} \frac{C_D}{C_f} \quad (2.5)$$

where g_m is the transconductance, τ_{sh} is the shaping time. Among the disadvantages coming from this large input capacity there is a coupling between the sensor and the electronics resulting in cross talk noise on neighbouring electrodes; indeed, since digital switching in the FE electronics does a lot of oscillations, this problem is especially connected with the intra wells capacities. So, larger charge collection electrode sensors provide a uniform electric field in the bulk that results in short drift path and so in good collection properties, especially after irradiation, when trapping probability can become an issue.

The small fill-factor variant, instead, benefits from a small capacity (5 fF to 20 fF), but suffers from a non uniform electric field and from all the issue related to that (slowness and high trapping probability). As we'll see these two different types of sensor require different amplifier: the large elcrtrode one is coupled with a charge sensitive amplifier, while the small one with a voltage amplifier (sec 2.5.1).

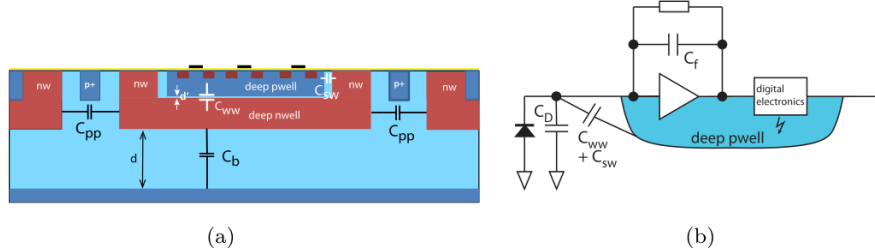


Figure 2.5: C_{pp} , C_b , C_{WW} , C_{SW}

	small fill factor	large fill factor
small sensor C	✓ (< 5 fF)	✗ (~ 100 200 fF)
low noise	✓	✗
low cross talk	✓	✗
velocity performances	✓	✗ (~100 ns)
short drift paths	✗	✓
radiation hard	✗	✓

Table 2.1: Small and large fill factor DMAPS characteristics

254 2.4.2 A modified sensor

255 A process modification, developed by CERN in collaboration with the foundries, which
 256 has become the standard solution to combine the characteristics of a small fill factor
 257 sensor (small input amplifier capacity) and of a large fill factor sensor (uniform electric
 258 field), is the one carried out for ALICE upgrade about ten years [1]. A compromise
 259 between the two sensors could also be making smaller pixels, but this solution requires
 260 reducing the electronic circuit area, so a completely new pixel layout should be though.
 261 The modification consists in inserting a low dose implant under the electrode and one of
 262 its advantage lies in its versatility: in fact, both standard and modified sensor are often
 263 produced for testing.

264 Before the process modification, the depletion region extends below the diode towards
 265 the substrate, and it does not extend much laterally, even if a high bias is applied to the
 266 sensor (fig. 2.6). After the modification, two distinct pn junctions are built: one between
 267 the deep p well and the n⁻ layer, and the other between the n⁻ and the p⁻ epitaxial
 268 layer, extending to the whole area of the sensor. Since deep p well and the p-substrate are
 269 separated by the depletion region, the two p electrodes can be biased separately² and this
 270 is beneficial to enhance the vertical electric field component. The doping concentration is
 271 a trimmer parameter: it must be high enough to be greater than in the epitaxial layer in
 272 order to prevent the punchthrough between p-well and the substrate, but it must also be
 273 low enough to allow the depletion for reasonable bias values.

²This is true in general, but it can be denied if other doping characteristics are implemented, and we will see that this is the case of TJ-Monopix1

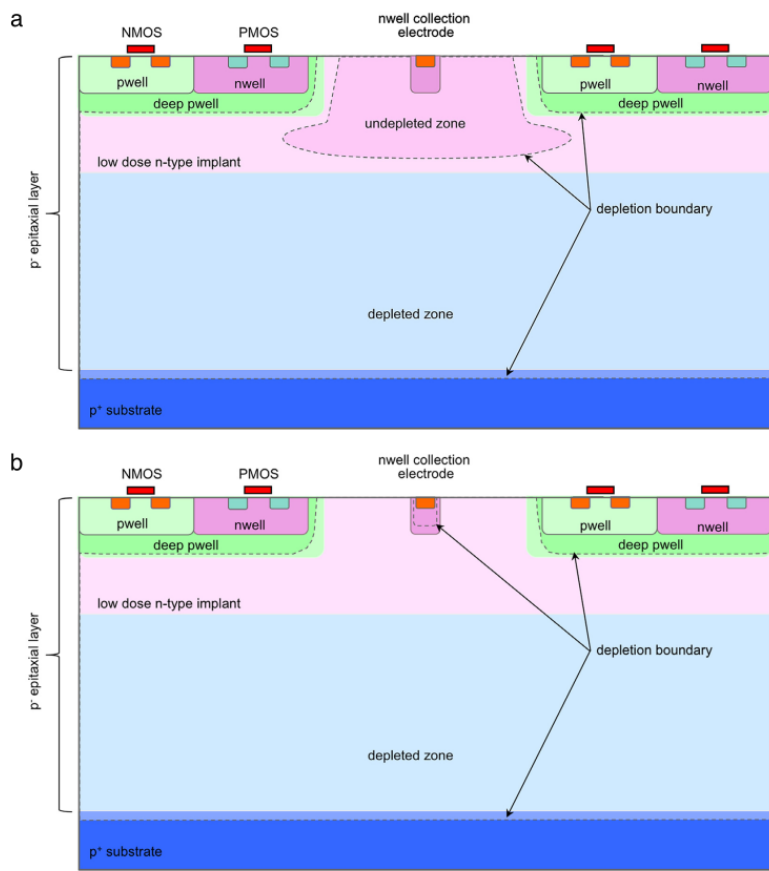


Figure 2.6: A modified process for ALICE tracker detector: a low dose n implant is used to create a planar junction. In (a) the depletion is partial, while in (b) the pixel is fully depleted.

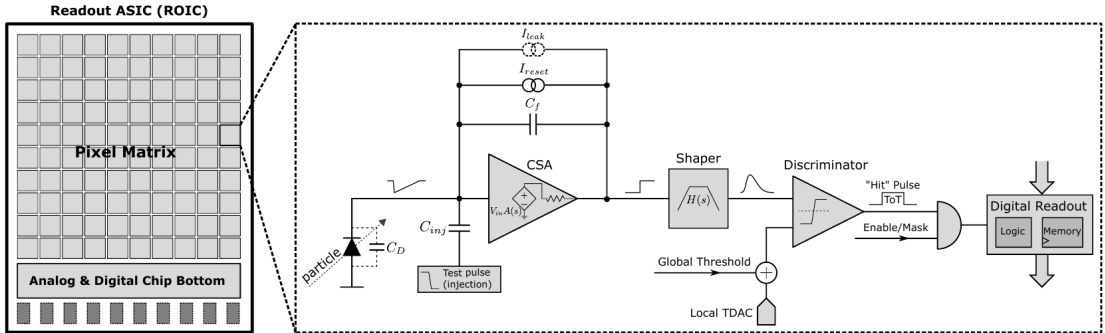


Figure 2.7: Readout FE scheme: in this example the preamplifier is a charge sensitive one (CSA) but changing the capacitive feedback into a resistive one, this can be converted in a voltage or current amplifier.

2.5 Analog front end

After the creation of a signal on the electrode, the signal enters the front end circuit (fig.2.7), ready to be molded and transmitted out of chip. Low noise amplification, fast hit discrimination and an efficient, high-speed readout architecture, consuming as low power as possible, are the goal of the readout integrated electronics (ROIC). The main parts of the analog front end chain are a preamplifier (that often is the only amplification stage) with a reset to the baseline mechanism and a leakage current compensation, a shaper (a band-pass filter) and finally a discriminator. The whole chain must be optimized and tuned to improve the S/N ratio. It is very important both not to have a large noise before the amplification stage in order to not multiply that noise, and chose a reasonable threshold of the discriminator to cut noise-hits much as possible.

2.5.1 Preamplifier

Even if circuits on the silicon crystal are only constructed by CMOS, a preamplifier can be processed as an operational amplifier (OpAmp) where the gain is determined by the input and feedback impedance (first step in figure 2.7):

$$G = \frac{v_{out}}{v_{in}} = \frac{Z_f}{Z_{in}} \quad (2.6)$$

Depending on whether a capacity or a resistance is used as feedback, respectively a charge or a voltage amplifier is used: if the voltage input signal is large enough and has a sharp rise time, the voltage sensitive preamplifier is preferred. Consequently, this flavor doesn't suit to large fill factor MAPS whose signal is already high enough: $v_{in} = Q/C_D \approx 3 \text{ fC}/100 \text{ pF} = 0.03 \text{ mV}$, but it's fine for the small fill factor ones: $v_{in} = Q/C_D \approx 3 \text{ fC}/3 \text{ pF} = 1 \text{ mV}$.

In the case of a resistor feedback, if the signal duration is longer than the discharge time ($\tau = R_S C_D$) of the detector the system works as current amplifier, as the signal is immediately transmitted to the amplifier; in the complementary case (signal duration longer than the discharge time) the system integrates the current on the C_D and operates as a voltage amplifier.

300 2.6 Readout logic

301 The readout logic includes the part of the circuit which takes the FE output signal, pro-
 302 cesses it and then transmit it out of pixel and/or out of chip; depending on the situation
 303 of usage different readout characteristics must be provided. To store the analogical in-
 304 formation (i.e. charge collected, evolution of signal in time, ...) big buffers and a large
 305 bandwidth are needed; the problem that doesn't occur, or better occur only with really
 306 high rate, if one wants record only digital data (if one pixel is hit 1 is recorded, and if not
 307 0 is recorded).

308 A common compromise is to store the time over threshold (ToT) of the pulse in clock
 309 cycle counts; this needs of relatively coarse requirement as the ToT can be trimmed down
 310 to use only a dozen bits but, being correlated (and hopefully linear) with the deposited
 311 charge, it provides a sufficient information. The ToT digitalization usually takes advantage
 312 of the distribution of a clock (namely BCID, bunch crossing identification) on the pixels'
 313 matrix. The required timing precision is better than ~ 25 ns, that corresponds to the period
 314 between bunch collisions at LHC; for such reason a reasonable BCID-clock frequency for
 pixels detector is 40 MHz.

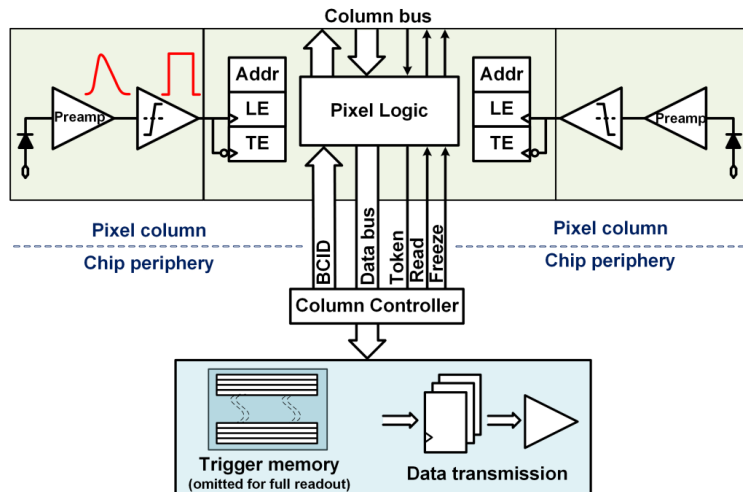


Figure 2.8: Column drain R/O scheme where ToT is saved

315 Moreover, the readout architecture can be full, if every hit is read, or triggered, if a
 316 trigger system decides if the hit must be stored or not. On one hand the triggered-readout
 317 needs buffers and storage memories, on the other the full readout, because there is no
 318 need to store hit data on chip, needs an high enough bandwidth. A triggered readout is
 319 fundamental in accelerator experiments where the quantity of data to store is very large
 320 and some selection has to be applied by the trigger: to give an order of magnitude, at LHC
 321 more than 100 TBit/s of data are produced, but the storage limit is about 100 MBit/s
 322 [2](pag. 797). Typically, the trigger signal is processed in a few μs , so the pixel gets it
 323 only after a hundred clock cycles from the hit arrival time: the buffer depth must be able
 324 to handle such high trigger latency.

325 After having taken out the data from the pixel, it has to be transmitted to the end
 326 of column (EoC) where a serializer delivers it out of chip, typically to an FPGA. There
 327 are several ways of transmitting data from a pixel to the EoC: one of the most famous
 328 is the column-drain read out, developed for CMS and ATLAS experiments [3]. All the

330 pixels in a double-column share a data bus and only one pixel at a time, according to
 331 a priority chain, can be read. The reading order circuit is implemented by shift register
 332 (SR): when a hit arrives, the corresponding data, which can be made of timestamp and
 333 ToT, is temporarily stored on a RAM until the SR allows the access to memory by data
 334 bus. Even if many readout architectures are based on the column-drain one, it doesn't suit
 335 for large size matrices. The problem is the increasing number of pixels on a column would
 336 also raise the number of pixels in the priority chain, which would result in a slowdown of
 337 the readout.

338 If there isn't any storage memory, the double-column behaves as a single server queue
 339 and the probability for a pixel of waiting a time T greater than t , with an input hit rate
 340 on the column μ and an output bandwidth B_W is [4]:

$$P(T > t) = \frac{\mu}{B_W} e^{-(B_W - \mu)t} \quad (2.7)$$

341 To avoid hit loss (let's neglect the contribution to the inefficiency of the dead time τ due
 342 to the AFE), for example imposing $P_T > t \sim 0.001$, one obtains $(B_W - \mu) t_t \sim 6$, where
 343 t_t is the time needed to transfer the hit; since t_t is small, one must have $B_W \gg \mu$, that
 means a high bandwidth [4].

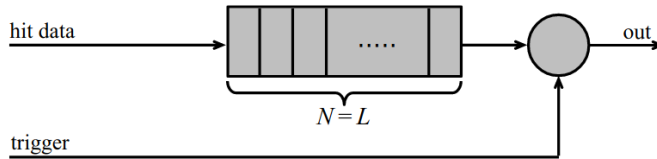


Figure 2.9: Block diagram of a pipeline buffer: N is the dimension of memory buffer and L is the trigger latency expressed in BCID cycles

344 Eq.2.7 is actually an approximation, since each pixel sees a different bandwidth de-
 345 pending on the position on the queue: the first one sees the full bandwidth, while the next
 346 sees a smaller one because it can be occasionally blocked by the previous pixel. Then,
 347 the bandwidth seen by the pixel i is $B_i = B - \sum_j \mu_j$, where μ_j is the hit rate of the j th
 348 pixel. The efficiency requirement on the bandwidth and the hit rate becomes: $B_{W,i} > \mu_i$,
 349 where the index i means that the constraint is for a single pixel; if all the N pixels on a
 350 column have the same rate $\mu = N\mu_i$, the condition reduces to $B_W > \mu$. The bandwidth
 351 must be chosen such that the mean time between hits of the last pixel in the readout chain
 352 is bigger than that. In order to reduce the bandwidth, a readout with zero suppression
 353 on pixel is typically employed; this means that only information from channels where the
 354 signal exceeds the discriminator threshold are stored.

356 If, instead, the signal is locally stored until a trigger signal arrives, the input rate to
 357 column bus μ' is reduced compared to the hit rate μ as: $\mu' = \mu \times r \times t$, where r is the
 358 trigger rate and t is the bunch crossing period. In this situation there is a more relaxed
 359 constraint on the bandwidth, but the limiting factor is the buffer depth: the amount of
 360 memory designed depends both on the expected rate μ and on the trigger latency t as
 361 $\propto \mu \times t$, which means that the higher the trigger latency the lower the hit rate to cope
 362 with.

363 In order to have an efficient usage of memory on pixels' area it's convenient grouping
 364 pixels into regions with shared storage. Let's compare two different situations: in the first
 365 one a buffer is located on each pixel area, while in the second one a core of four pixels

366 share a common buffer (this architecture is commonly called FE-I4).

Consider a 50 kHz single pixel hits rate and a trigger latency of 5 μs , the probability of

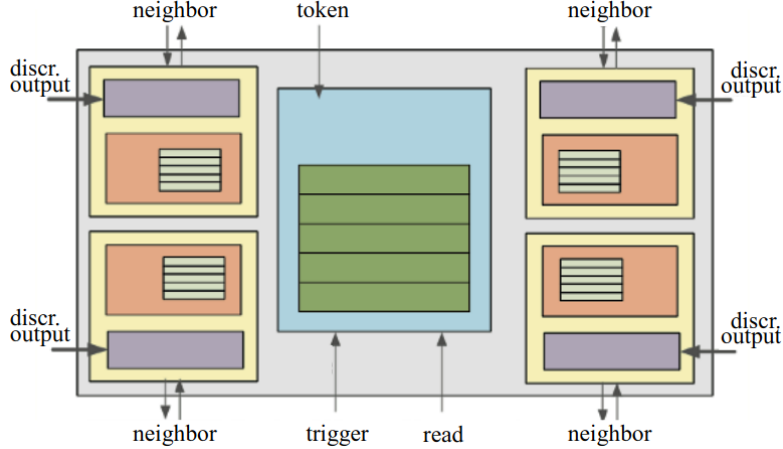


Figure 2.10: Block diagram of the FE-I4 R/O. Read and memory management section is highlighted in light blue; latency counters and trigger management section are highlighted in green; hit processing blocks are highlighted in purple; ToT counters and ToT management units are highlighted in orange

367

368 losing hits is:

$$P(N > 1|\nu) = 1 - P(N = 0|\nu) - P(N = 1|\nu) = 1 - e^{-\nu}(1 + \nu) \approx 2.6\% \quad (2.8)$$

369 where I have assumed a Poissonian distribution with mean $\nu = 0.25$ to describe the counts
370 N.

371 To get an efficiency ϵ greater than 99.9 % a 3 hit depth buffer is needed:

$$P(N > 3|\nu) = 1 - \sum_{i=0}^3 P(N = i|\nu) < 0.1\% \quad (2.9)$$

372 Consider the second situation: if the average single pixel rate is still 50 kHz, grouping four
373 pixels the mean number of hits per trigger latency is $\nu = 0.25 \times 4 = 1$. To get an efficiency
374 of 99.9% (eq. 2.9) a buffer depth of 5 hits in the four-pixels region, instead of 3 per pixels,
375 is needed.

³⁷⁶ **Chapter 3**

³⁷⁷ **Use of pixel detectors**

³⁷⁸ There always was a tight relation between the development of cameras and pixel detectors since 1969, when the idea of CCDs, thanks to whom Boyle and Smith were awarded
³⁷⁹ the Nobel Prize in Physics in 2009, revolutionized photography allowing light to be captured electronically instead of on film. Even though the CMOS technology was already
³⁸⁰ known when CCDs spread, the costs of productions were too high to allow the diffusion
³⁸¹ of these sensors for which would take almost 20 years. From that period on, the
³⁸² fast diffusion of CMOS was mainly due to the less cost than CCD, and the less power
³⁸³ supply required. Nowadays CCDs are still preferred over MAPS in astronomy, where the
³⁸⁴ astronomical sources' rate are low enough to cope with slow readout time (tens of ms).
³⁸⁵

³⁸⁶ The principal use cases of pixel detectors are particle tracking and imaging: in the
³⁸⁷ former case individual charged particles have to be identified, in the latter instead an
³⁸⁸ image is obtained by the usually un-triggered accumulation of the impinging radiation.
³⁸⁹ Also the demands on detectors performance depends on their usage, in particular tracking
³⁹⁰ requires high spatial resolution, fast readout and radiation hardness.
³⁹¹

³⁹² **3.1 Tracking in HEP**

³⁹³ At first the physics world overlooked the CCDs, and all pixel in general, as against the
³⁹⁴ gaseous detector for tracking: there was no need to replace these ones which had a sufficient
³⁹⁵ good resolution ($100\mu\text{m}$). Since 1974, with the measurement of the invariant mass of the
³⁹⁶ J/Psi and the affirmation of the quark model, all experiments start to look for better
³⁹⁷ spatial resolutions in order to achieve the possibility of reconstructing short lived particle.

³⁹⁸ Historically, the first pixel detector employed in particle physics was a CCD: it was
³⁹⁹ installed in the spectrometer at the CERN's Super Proton Synchrotron (SPS) by the
⁴⁰⁰ ACCMOR Collaboration (Amsterdam, CERN, Cracow, Munich, Oxford, RAL) at mid
⁴⁰¹ 1980s, with the purpose of studying the (at the time) recently-discovered charm particles.
⁴⁰² The second famous usage of CCDs took place at SLAC in the Large Detector (SLD) during
⁴⁰³ the two years 1996-98, where the CCD technology was adopted instead of the microstrip
⁴⁰⁴ detectors for their excellent spatial resolution (cell size $22\times 22\mu\text{m}^2$ giving a resolution of
⁴⁰⁵ $\sim 5\mu\text{m}$) thanks to the sufficient time for readout between two successive collisions (160 ms).

⁴⁰⁶ From that period on particle tracking in experiments have been transformed radically:
⁴⁰⁷ it was mandatory for HEP experiments to build an inner vertex detector, where the general
⁴⁰⁸ tasks are:

- ⁴⁰⁹ • pattern recognition with the identification of particle tracks at large backgrounds and

410 pile-up

- 411 • measurement of vertices (primary and secondary)
- 412 • multi-track and vertex separation in the core of jets
- 413 • measurement of specific ionization
- 414 • momentum measurement combining with other detectors informations

415 In 1991, the more demanding environments led to the development of hybrid pixel
416 detectors: a dedicated collaboration, RD19, was established at CERN with the specific goal
417 of defining a semiconductor micropattern detector with an incorporated signal processing
418 at a microscopic level. In those years a wide set of prototypes of hybrid pixel has been
419 manufactured; among the greatest productions a mention goes to the huge ATLAS and
420 CMS vertex detectors. From the middle of 2013 a second collaboration, RD53, has been
421 established with the new goal of finding a pixel detector suitable for phase II future
422 upgrades of those experiments. Even if the collaboration is specifically focused on design
423 of hybrid pixel readout chips (aiming to 65 nm tecnique so that the electronics fits within
424 the pixel area), also other options have been taken in account and many test have been done
425 on MAPS. Requirements imposed by HL-LHC will become tigher in time: for example, a
426 dose and radiation of 5 Mrad and 10^{16} NIEL are exepected after 5 years of operation. Time
427 resolution, material budget and power consumption are also issues for the upgrade: to
428 distinguish different events from different bunches a time resolution better than 25 ns for
429 a bunch crossing frequency of 40 MHz is required, and also a material budget lower than
430 2% and a power consuption lower than 500 mW/cm² are required.

431 Amidst the solutions proposed 3D silicon detector, invented by Sherwood Parker in
432 1995, and MAPS are the most promising. In 3D sensors the electrode is a narrow column
433 of n-type implanted vertically across the bulk instead of being implanted on the wafer's
434 surface. The charge produced by the impinging particle is then drifted transversally within
435 the pixel, and, as the mean path between two electrode can be souffcient low, the trap
436 probability is not an issue. Even if 3D detector are adequately radiation hard and are a
437 strong contender for hybrid pixel modules, especially in the innermost pixel detector layer,
438 the fabrication process is currently low volume, making them unlikely to cover large areas.

439 3.1.1 Hybrid pixels at LHC and at SuperKEKB

440 **ATLAS**

441 With CMS, ATLAS is one of two general-purpose detectors at the LHC and has the largest
442 volume detector ever constructed for a particle collider (46 m long and 25 m in diameter).
443 The Inner Tracker (ITk) consists of three different systems all immersed in a magnetic
444 field parallel to the beam axis whose main components are: the pixel, the micro-strips and
445 transition radiation trackers. Concerning the pixel detector, they installed a 3-layer hybrid
446 pixel detector in 2007 and an additional one inserted within the original detector envelope
447 and therefore called insertable B-layer (IBL) in 2014. 92 million pixels are divided in 4
448 barrel layers and 3 disks in each end-cap region, covering a total area of 1.9 m² and having
449 a 15 kW of power consumption.

450 As stated by the ATLAS collaboration the pixel detector is exposed by an extreme
 451 particle flux: "By the end of Run 3¹, the number of particles that will have hit the
 452 innermost pixel layers will be comparable to the number it would receive if it were placed
 453 only a few kilometres from the Sun during a solar flare". Considering that the particle
 454 density will increase even more with HL-LHC, radiation hardness is definitively target to
 455 achieve. The most ambitious goal is employ a MAPS-based detector for the inner-layer
 456 barrels, and for this reason the RD53 collaboration is designing many MAPS prototypes
 457 (as for example TJ-Monopix1, which I will talk about in chapter 4) and performing test.
 458 Up to now this possibility will be eventually implemented during the second phase of the
 459 HL-LHC era, as at the start of high-luminosity operation the selected option is the hybrid
 460 one. The sensor will be bonded with ITkPix, the first full-scale 65 nm hybrid pixel-readout
 461 chip developed by the RD53 collaboration. Regarding the sensor, a valuable option is
 462 using 3D pixels, which have already proved themselves in ATLAS, for the IBL, where they
 463 were introduced in a limited acceptance range and introduced a new readout integrated
 464 circuit called FE-I4. Also the complexity of the readout will be raised, as the number of
 465 pixels will be increased of a factor about 7, passing from 92 millions to 6 billion.

466 CMS

467 **da scrivere** hybrid pixel detector 124 million pixels; cylindrical layers roughly at 3cm, 7cm,
 468 11cm and 16cm (upgrade in 2017, prima ne avevano 3 di layer) and disks at either end,
 469 and so will be vital in reconstructing the tracks of very short-lived particles. Each of
 470 these silicon pixels is 100um by 150um, even with only around 50 microwatts per pixel, the
 471 total power output is 7.5kW- The upgrade baseline ROIC was redesigned for the outer
 472 3 layers, replacing analog signal readout with on-chip ADCs and digital readout at higher
 rate

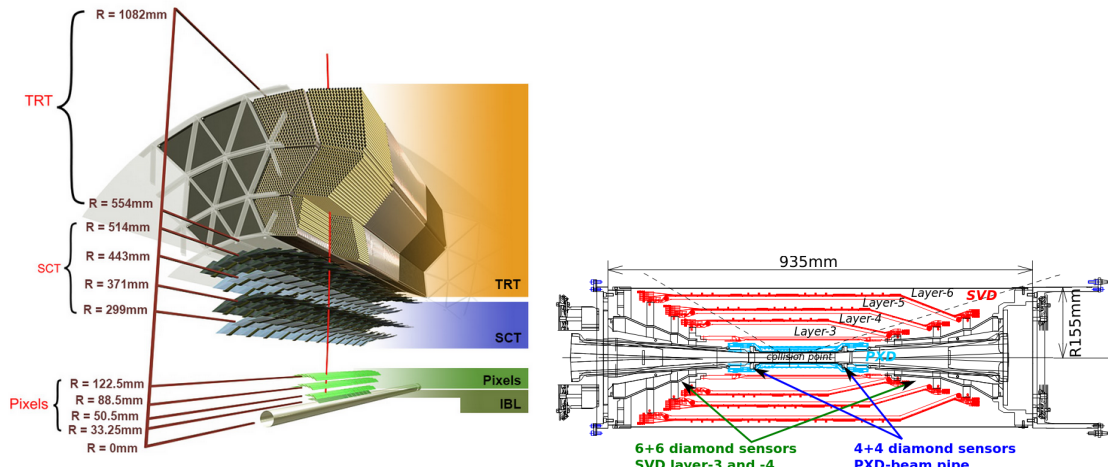


Figure 3.1: (a), (b) Since an accidental beam background enhancement can damage the VXD, diamond detectors are installed in order to monitoring it.

473

¹Run 3 start in June 2022

474 **LHCb**

475 LHCb is a dedicated heavy-flavour physics experiment that exploits pp interactions at
476 14 TeV at LHC. It was the last experiment to upgrade the vertex detector, the Vertex
477 Locator (VELO), replacing the silicon-strip with 26 plane pixel detector (because of the
478 fixed target geometry) in May 2022. As the instantaneous luminosity in Run3 is increased
479 by a factor $\lesssim 10$, much of the readout electronics and of the trigger system have been
480 developed in order to cope with the large interaction rate. To place the detector as close as
481 possible to the beampipe and reach a better track reconstruction efficiency and resolution,
482 the VELO has a surprising feature: during the injection of LHC protons it is parked at
483 3 cm from the beams and only when the stability is reached it is moved at ~ 5 mm. Readout
484 speed is a priority for the detector that uses a triggerless readout at 40 MHz collision rate,
485 producing 20 Gbps per ROIC. The Velopix, which is the hybrid system designed for LHCb,
486 is made of bonding sensors, each measuring 55×55 micrometers, 200 μm -thick to a 200 μm -
487 thick ASIC specially developed for LHCb and coming from the Medipix family (sec. ??),
488 which can handle hit rates up to 900 MHz per chip. Since the detector is operated under
489 vacuum near the beam pipe, the heat removal is particularly difficult and evaporative CO₂
490 microchannel cooling are used.

491 **BelleII**

492 The current vertex detector of BelleII, VXD, is made of a pixel detector (PXD), fabricated
493 with 2 layers of DEPFET-based pixels, and 4 layers of a double-sided silicon strip detectors
494 (SVD)[5]. Due to the small capacitance of the collection node, DEPFET presents a high
495 signal-to-noise ratio (in 30-50) thanks to the low intrinsic noise and to the large signal
496 achieved with the fully depleted bulk: pixels are thinned to 75 μm in the active region,
497 then a MIP is supposed to create a signal of $\sim 6000 e^-$, while the typical noise of DEPFET
498 is around $200 e^-$. The ASIC read out is still based on a rolling shutter logic, with an
499 integration time of 20 μs . In order to reduce the data-storage memory PXD hits are only
500 used to improve spatial resolution of tracks: the SVD informations are used by the High
501 Level Trigger (HLT) to look for regions of interest in the pixel ladders just by extrapolating
502 back the tracks found in the tracker detector, and this method allows to store only data
503 belonging to these areas; the PXD hits are then used in offline track fit to improve the
504 vertex resolution.

505 MAPS have been proposed for the replacement of VXD during the Long Shut Down
506 2 (LSD2) foreseen around 2026-27; the new vertex detector, VTX, should be made of 5
507 layers fabricated by the optimized Belle II pixel sensor (OBELIX), a detector based on
508 TJ-Monopix have been selected (look at chapter ??). The main advantages VTX should
509 bring are a obvious improvement in the track and vertex resolution (14 μm before upgrade,
510 $\lesssim 10 \mu\text{m}$ expected after upgrade) and a reduction in the X_0 (da.. a..), a higher background
511 tolerance because of the smaller sensor than strips dimension and a low bandwidth due to
512 the on-chip sparsification.

513 **3.1.2 First attempts to MAPS**

514 **MIMOSA at EUDET and STAR**

515 epilayer not fully depleted, charge collection mostly by diffusion, typical collection time
516 bigger than 100 ns. Correlated Double Sampling MIMOSA [6][7] (standing for Minimum

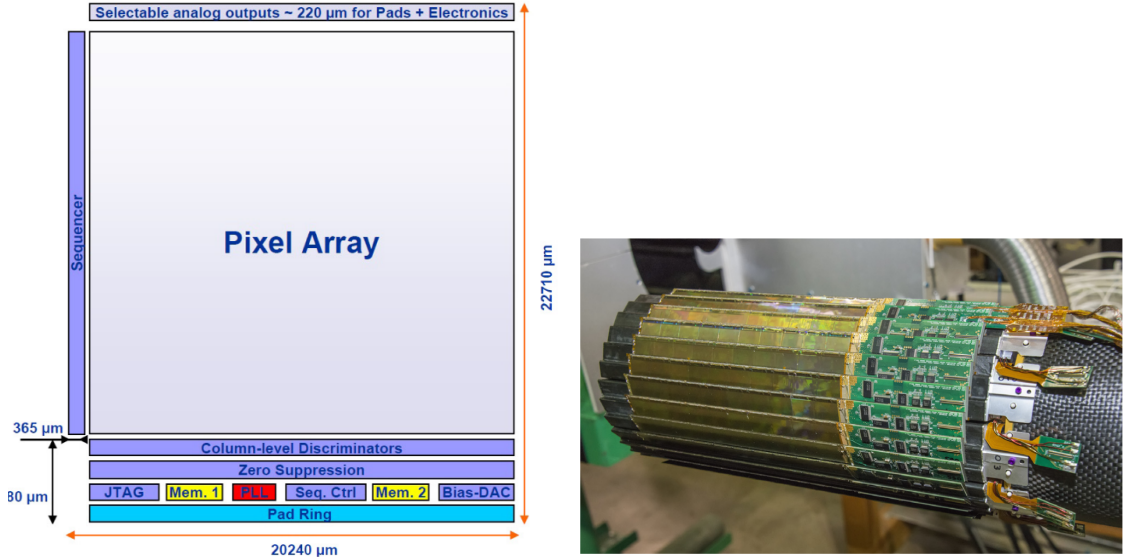


Figure 3.2: (a) The HFT PXL detector; (b) Block-diagram of the ULTIMATE-2 sensor

517 Ionizing MOS Active pixel sensor), designed in 2008, prefigured the architecture of MAPS
 518 for coming vertex detector being the first large scale sensor to be employed as detector.
 519 MIMOSA-26 equiped the final version of EUDET high resolution beam telescope both at
 520 CERN-SPS and at DESY while the MIMOSA-28 devices are used for the first MAPS-
 521 based vertex detector at the STAR experiment. MIMOSA-26 is fabricated in a 350 nm,
 522 and a module features 1152 columns, split into 18 indipendent groups, and 576 rows, with
 523 square pixels having a side of 18.4 μm lenght; therefore, because of the small dimension,
 524 charge sharing is an issue aggiungi qualcosa. The readout is done in a rolling shutter
 525 mode: the chip is an Active Pixels (APS) and therefore it incorporates the amplification
 526 on pixel, while the signal discrimination and zero-suppression (primo chip with integrated
 527 zero suppression) logic are placed at the EoC, where is also placed a memory. The chip
 528 is an Active Pixels (APS) and therefore it incorporates the amplification on pixel, while
 529 the signal discrimination and zero-suppression logic are placed at the EoC: the readout is
 530 done in a rolling shutter mode with a frame integration time that can be lowered down to
 531 85 ms, and a memory allowing to store up to six hits is.

532 The EUDET telescope, equipped with six sensor planes, requires highly granular and
 533 thin pixel detectors in order to achieve an excellent track resolution (around 2 μm) even at
 534 the rather low particle energies of up to 6 GeV. The STAR experiment at the Relativistic
 535 Heavy Ion Collide (RHIC) accelerator at the Brookhaven National Laboratory (BNL) is
 536 the first to include MAPS in the vertex detector[8]. The main tracking detector in STAR is
 537 a TPC with radii 60-190 cm embedded in a 0.5 T solenoidal magnetic field, that provides
 538 a pointing resolution of approximately 1 mm. The pixel detector, PXL, is a part of a
 539 3-detector system, Heavy Flavor Tracker (HFT), that has been added to the pre-existing
 540 STAR apparatus just before the 2014 Run in order to improve the impact parameter
 541 resolution and to enable the direct reconstruction of hadronic decays of heavy flavor mesons
 542 and baryons. The Heavy Flavor Tracker (HFT) is composed by the Silicon Strip Detector
 543 (SSD), the Intermediate Silicon Tracker (IST) and the Pixel Detector (PXL); the first
 544 one is placed at 22 cm from the beam pipe and consists of double sided strips with 95 μm
 545 inter-strip pitch, the second one, placed at 14 cm, is made of single sided silicon pads

546 with $600\text{ }\mu\text{m} \times 6\text{ mm}$ pitch and the last one made by two layers is placed at 2.8 cm and 8 cm
 547 fabricated with ULTIMATE2 (also known as MIMOSA-28), a successor of MIMOSA-26
 548 sensor, with pitch $20.7\text{ }\mu\text{m}$ and thinned down to $50\text{ }\mu\text{m}$. An area of 0.16 m^2 are covered
 549 by 400 MAPS sensor, corresponding to 356 milions of pixels divided into array size of 928
 550 $\times 960$. Each pixel includes circuitry for readout, amplification, and Correlated Double
 551 Sampling (CDS) for signal extraction and noise subtraction and the frame integration time
 552 is $185.6\text{ }\mu\text{s}$; after the subtraction the signal to noise ratio is ~ 30 , with a noise between
 553 10-12 electrons and a signal of 1000 e^- . Thanks to the HFT system and the PXL, STAR
 554 achieved a track pointing resolution $46\text{ }\mu\text{m}$ for 750 MeV/c kaons, and better than $30\text{ }\mu\text{m}$ for
 555 particle momenta bigger than 1 GeV/c : this performance enabled the study of D-meson
 556 production with a high significance signal.

557 ALPIDE at ALICE

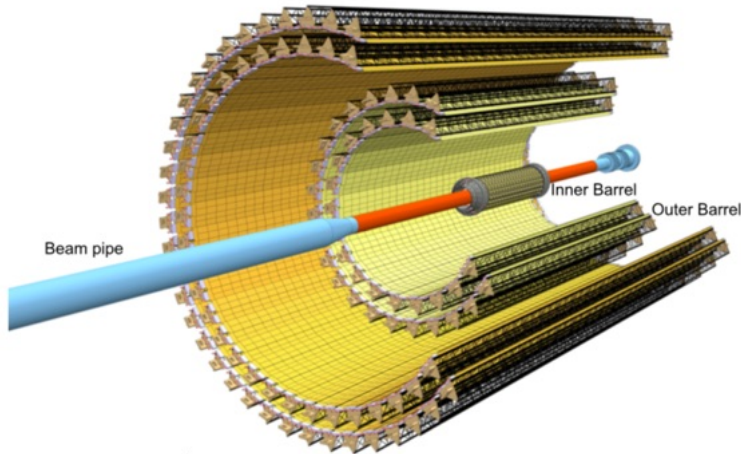


Figure 3.3

558 ALICE Tracking System (ITS2), upgraded during the LHC long shut down in 2019-20,
 559 was the first large-area ($\sim 10\text{ m}^2$ covered by 2.5 Gpixels) silicon vertex detector based on
 560 CMOS MAPS.

561 ALICE (A Large Ion Collider Experiment) is a detector dedicated to heavy-ion physics
 562 and to the study of the condensed phase of the chromodynamics at the LHC. The tracking
 563 detector consists of the Inner Tracking System (ITS), the gaseous Time Projection Cham-
 564 ber (TPC) and the Transition Radiation Detector (TRD), and all those are embedded in
 565 a magnetic field of 0.5 T . The ITS is made by six layers of detectors, two for each type,
 566 from the interaction point outwards: Silicon Pixel Detector (SPD), Silicon Drift Detector
 567 (SDD) and Silicon Strip Detector (SSD). Contrary to the others LHC experiments, AL-
 568 ICE tracker in placed in a quite different environments: the expected dose is smaller by
 569 two order of magnitude and the rate of interactions is few MHz instead of 40 MHz, but
 570 the number of particles comes out of each interaction is higher (the SPS is invested by a
 571 density of particles of $\sim 100\text{ cm}^{-2}$). The reconstruction of very complicated events whit a
 572 large number of particle is a challenge, hence to segment and to minimize the amount of
 573 material, which may cause secondary interaction complicating futher the event topology, is
 574 considered a viable strategy. The detector employs the ALPIDE chip, developed by AL-
 575 ICE collaboration, fabricated in the 180 nm CMOS Imaging Sensor process of TowerJazz,

whose design takes full advantage of process feature which allows full circuitry within the pixel matrix. Thanks to the reduction of the material budget, ITS2 obtained an amazing improvement both in the position measurement and in the momentum resolution, improving the efficiency of track reconstruction for particle with very low transverse momentum (by a factor 6 at $pT \sim 0.1$ GeV/c). Further advancements in CMOS MAPS technology are being aggressively pursued for the ALICE ITS3 vertex detector upgrades (foreseen around 2026-27), with the goals of further reducing the sensor thickness and improving the readout speed of the devices, while keeping power consumption at a minimum.

charge collection time <30ns Asynchronous matrix readou

3.2 Other applications

Historically for imaging purpose the CCDs were the favoured device: they can be used as single photon counter or integrating and collecting the charge released by more impinging particles. The utilisation in the first case is similar to the tracking one, except that the requirements are less tight, so much that two noteworthy of microchips originally meant for detectors in particle physics at the LHC, and later employed in other fields are Medipix and Timepix. They are read-out chips developed by the Medipix Collaborations since early 1990s. For two decades, different Medipix generations have been produced, having a rough correlation with the feature size used: Medipix2 (1999) used 250 nm feature size CMOS while Medipix3 (2005) 130 nm. For photons imaging other materials with higher atomic charge than silicon could be prefered, as a high photon absorption efficiency is needed: it was for this reason that Medipix2 was bump bonded to identically segmented sensors of both silicon and GaAs.

The applications in scientific imaging vary from astrophysics and medical imaging to more exotic domains as studies of protein dynamics, art authentication and dosimetry. The most important employment of Medipix is as X-ray single photon counting in industrial and medical radiography and in 3D computed tomography. Thanks to a New-Zealand company, the MARS Bioimaging detector has been fabricated, which is capable of resolving the photons energy and produce 3D coloured images. Besides tracking in HEP (I have already cited the use of Timepix3 in the beam telescope of the LHCb VELO), an important use of Timepix is in dosimetry [Timepix Detector for Imaging in Ion Beam Radiotherapy- aggiungi qualche info](#) A small-Timepix detector with the dimension of a USB can also be found at the International Space Station, where it is exploited for radiation, principally made of heavy-ion, monitoring.

3.2.1 Applicability to FLASH radiotherapy

A possible new application of pixels detector is dosimetry or beam monitoring of charged particles in high intensity radiography. The radiological treatment is a common method used in 60% of tumors both as palliative care and as treatment. It can be given before, after or during a surgery, (Intra operative radiation therapy-IORT) and many different types of radiations (photons, electrons, protons and ions, which mainly are hydrogen and carbon) can be used to irradiate the affected tissues. Exploiting the ionizing energy loss, that can be parametrized by the Linear Energy Transfer (LET), a biological damage can be delivered to the tissue: while α and β particles are high LET radiations with values in 100 keV/ μ m to 200 keV/ μ m, x-rays and gamma-rays are low LET radiations with values

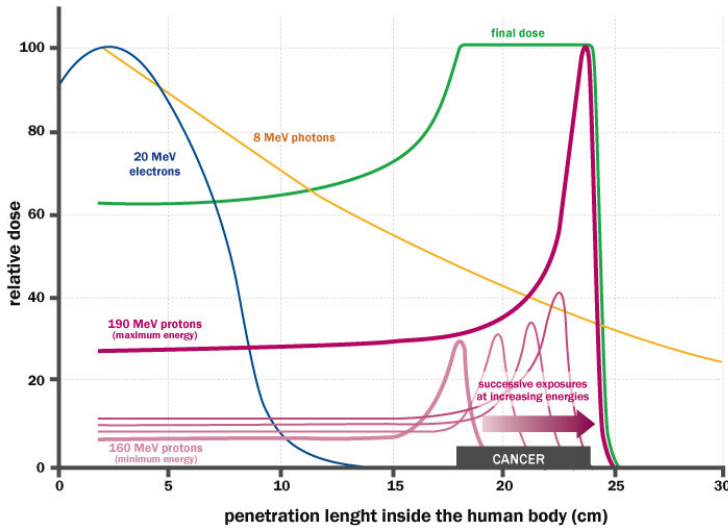


Figure 3.4: The Spread Out Bragg Peak (SOBP) curve (green), which is a constant dose distribution, is obtained from the superposition of many Bragg peak of hadrons with different energy.

619 in range $0.2 \text{ keV}/\mu\text{m}$ to $2 \text{ keV}/\mu\text{m}$.

620 If x-ray photons, with energy in 4 MeV to 25 MeV are used, the ionization is caused
 621 by the Compton electrons and is more in the superficial layers of the tissue due to the
 622 exponential attenuation of the beam. The hardrons energy loss, instead, is strongly lo-
 623 calized in the last region of the track, that is the Bragg peak. Ion beam enables better
 624 focusing of the radiation thereby improves the sparing of the surrounding healthy tissues;
 625 on the other hand the delivered dose distribution depends more on the patient's density
 626 tissues (e.g. bones, swelling, fat). Ensuring the target coverage is a fundamental objective
 627 in radiotherapy and is closely connected to the choice of the particles. Electrons cover the
 628 target since they tend to spread out and can cover a field size of a few cm^2 at a distance of
 629 a few cm from the source. Instead, the limited size of the beam for protons and photons
 630 from ultra high dose rate microbeam radiation therapy (MRT), for which FLASH effect
 631 was seen, requires the scanning of target. The radiobiological consequences of scanning
 632 both in spatial-fractionation and in prolonged exposure, which might not be sufficient to
 633 maintain a high mean dose rate to trigger FLASH effect, need to be explored. To date,
 634 the FLASH effect has been most commonly demonstrated using low-energy electron linacs

635 Recently² a promising method for RT at ultra high dose rate (at least 40 Gy/s) and
 636 for this reason called FLASH-RT[9], instead of CONV-RT (0.03 Gy/s), came out. This
 637 treatment takes advantages of biological differences between tumors and healthy tissues:
 638 it is characterized by reducing normal tissue toxicity and maintaining equivalent tumor
 639 damage. The response to dose can be described by the survival fraction probability,
 640 describing the fraction of surviving cell as a function of the dose:

$$S(D) = S(0) e^{-(\alpha D + \beta D^2)} \quad (3.1)$$

²The first evidences has been observed on a mice experiments in 1966 and in 2014 by the group of Favaudon and Vozenin. After this, many test on cats and pigs have been performed, and also there has been a clinical trial on a cutaneous tumor-patient

	CONV-RT	FLASH-RT
Dose rate	0.03 Gy/s	40 Gy/s
Intra pulse dose rate	100 Gy/s	106 Gy/s
Treatment duration	~minutes	$\lesssim 500$ ms
DDP	0.3 mGy	1 Gy to 10 Gy
Pulse width	3 μ s	$\sim 2 \mu$ s

Table 3.1: Typical value of treatment parameters

641 where α and β respectively represents the rate of cell killing by single ionizing events and
 642 by double hits. Hence, at high doses the density of damages increases and the cells repair
 643 becomes more difficult. Even if the FLASH effect is not yet completely understood and
 644 the underlying mechanisms are not clear, it looks like there are two different recipes which
 645 are involved:

- 646 • **The dose rate:** higher dose rate produce bigger damages (fig. 3.5(a)) since this
 647 prevent cells from sparing.
- 648 • **The presence or absence of oxygen:** while hypoxic cells are very resistant to radi-
 649 ation, normal oxygenated cells are highly radiosensitive. This is because if molecules
 650 containing O_2 break due to the impinging radiation, then the oxygen can build Re-
 651 active Oxygen Species (ROS) (fig.3.5(b))

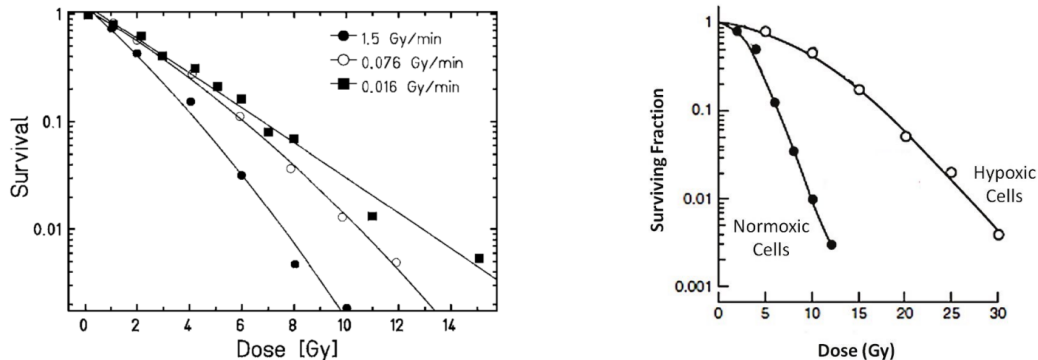


Figure 3.5: (a) Survival curve for different dose rate and (b) for different oxygen cell content

652 The Tumor Control Probability (TCP) and the Normal Tissue Complication (NTC)
 653 functions parametrize respectively the efficiency of damaging on the tumor after having
 654 released a certain dose and the probability of not affecting the healthy tissues. The
 655 intermediate zone between the increase of the TC and of the NTC is called therapeutic
 656 window, and the wider it is and the more effective the treatment is.

657 Dosimetric problems

658 Finding dosimeters suitable for online monitoring of the beam at ultra high dose rate is
 659 still an open issue since almost all standard online dosimeters show saturation problems.
 660 Differently, radiochromic films, which are the standard passive dosimeters, show dose-rate

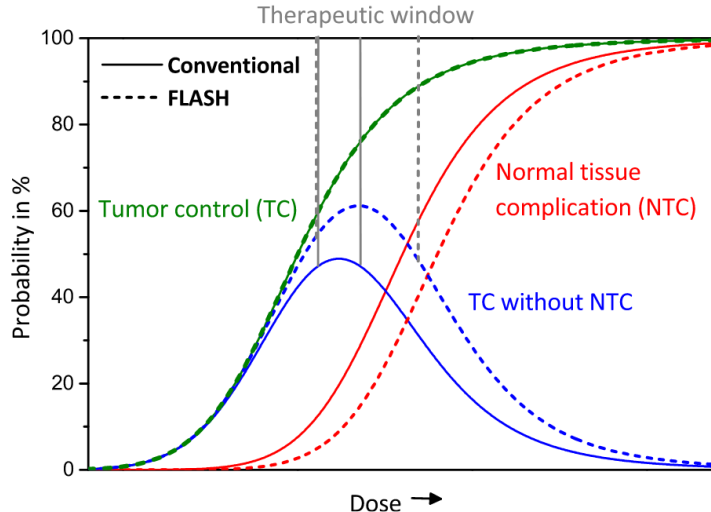


Figure 3.6: Illustration of dependence of TCP, NTCP and therapeutic window on dose, for CONV-RT ad FLASH-RT.

661 indipendece up to 109 Gy/s. **Cosa sono i radiochromic films and they do not have the same**
 662 **accuracy of other detectors.** The principal detectors for reference dosimetry which provide
 663 real-time dose measurement are Ionization Chambers (IC), that show saturation issue at
 664 dose per pulse (DDP) two orders of magnitude lower than the ones used for FLASH-RT.
 665 **da qui in poi** ICs devono essere calibrate secondo la metrologia , per cui grazie a protocollli
 666 di calibrazione e introducendo dei fattori correttivi si riesce a fare una misura di dose.
 667 k_{sat} which accounts for the loss of charge collected due to recombination. Doppi problemi
 668 sia di saturazione dovuta a ion recombination sia di scariche, must be carefully accounted
 669 for: questo doppio effetto è dato dal fatto che, creandosi tante cariche nella camera, che
 670 va ad annullare il campo elettrico di drift. Questo ovviamente paralizza le cariche che non
 671 driftano più, ma che anzi si ricombinano ed inoltre facilita la formazione di scariche. Per
 672 DDP minori di 1 mGy il fattore correttivo è minore al 5%, poi però aumenta substantially.

673 Scintillators have reusable, non-exhaustible scintillation centers. However, the system
 674 has a total deadtime given by both the crystal scintillation time and the electronics read-
 675 out deadtime.

676 Semiconductors show a nonreversible saturation beyond a threshold around 15 cGy/p.
 677 The scintillator used, shows a negligible saturation up to 1 Gy/p, but it increases signifi-
 678 cantly up to at least 11 Gy/p, and it reaches a cutoff value between 11 and 36 Gy/p.

679 Scintillator dosimeters are widely used in radiotherapy. They are usually operating in
 680 counting-mode where each detected signal is processed by read-out electronics. However,
 681 the system has a total deadtime given by both the crystal scintillation time and the
 682 electronics read-out deadtime When a scintillator dosimeter is used in integrator-mode
 683 the signal is integrated over the entire irradiation time.A deadtime, due to the decay time
 684 of the scintillating material, is considered on average every N recorded pulses, where N is
 685 the number of scintillation centres in the dosimeter.

686 Besides saturation two other requirements for online dosimeters are high temporal and
 687 space resolutions. **Si potrebbe pensare di poter usare i pixel detector as beam monitor**
 688 **che hanno risoluzioni spaziali anche inferiori al 10 um e ris temporali -qua dare un valore**
 689 **è più difficile perchè per i maps la risoluzione temporale dipende da l occupancy.** Uno dei

690 problemi è però il lungo dead time introdotto dal lungo tempo di readout (ricordiamo
691 che sopportano circa 100 Mhz/cm²).

692 Chapter 4

693 TJ-Monopix1

694 TJ-Monopix1 is a small electrode DMAPS with fast R/O capability, fabricated by Tow-
 695 erJazz foundry in 180 nm CMOS imaging process. It is part, together with prototypes
 696 from other series such as TJ-MALTA, of the ongoing R&D efforts aimed at developing
 697 DMAPS in commercial CMOS processes, that could cope with the requirements at ac-
 698 celerator experiments. Both TJ-Monopix and TJ-MALTA series [10], produced with the
 699 same technology by TowerJazz (the timeline of the foundry products is shown in figure
 700 4.1), are small electrode demonstrators and principally differ in the readout design: while
 701 Monopix implements a column-drain R/O, an asynchronous R/O without any distribution
 702 of BCID has been used by TJ-Malta in order to reduce power consumption.



Figure 4.1: Timeline in TowerJazz productions in 180 nm CMOS imaging process

703 Another Monopix series, but in 150 nm CMOS technology, has been produced by
 704 LFoundry [11]. The main differences between the LF-Monopix1 and the TJ-Monopix1
 705 (summarized in table 4.2), lay in the sensor rather than in the readout architecture, as
 706 both chips implements a fast column drain R/O with ToT capability [12][13]. Concerning
 707 the sensors, either are based on a p-type substrate, but with slightly different resistivities;
 708 in addition LFoundry pixels are larger, thicker and have a large fill factor (the very deep n-
 709 well covers ~55% of the pixel area). The primary consequence is that LF-Monopix1 pixels
 710 have a higher capacity resulting in higher consumption and noise. As I discussed in section
 711 2.4.1, the fact that LF-Monopix has a large fill factor electrode is expected to improve its
 712 radiation hardness. Indeed, a comparison of the performance of the two chips showed that
 713 TJ-Monopix suffers a comparatively larger degradation of efficiency after irradiation, due
 714 to the low electric field in the pixel corner; on the other hand, a drawback of the large fill
 715 factor in LF-Monopix is a significant cross-talk.

	LF-Monopix1	TJ-Monopix1
Resistivity	$>2 \text{ k}\Omega\text{cm}$	$>1 \text{ k}\Omega\text{cm}$
Pixel size	$50 \times 250 \mu\text{m}^2$	$36 \times 40 \mu\text{m}^2$
Depth	$100\text{-}750 \mu\text{m}$	$25 \mu\text{m}$
Capacity	$\sim 400 \text{ fF}$	$\sim 3 \text{ fF}$
Preamplifier	charge	voltage
Threshold trimming	on pixel (4-bit DAC)	global threshold
ToT	8 bits	6 bits
Consumption	$\sim 300 \text{ mW/cm}^2$	$\sim 120 \text{ mW/cm}^2$
Threshold	$1500 e^-$	$\sim 270 e^-$
ENC	$100 e^-$	$\sim 30 e^-$

Table 4.1: Main characteristics of Monopix1 produced by TowerJazz and LFoundry [12][13]

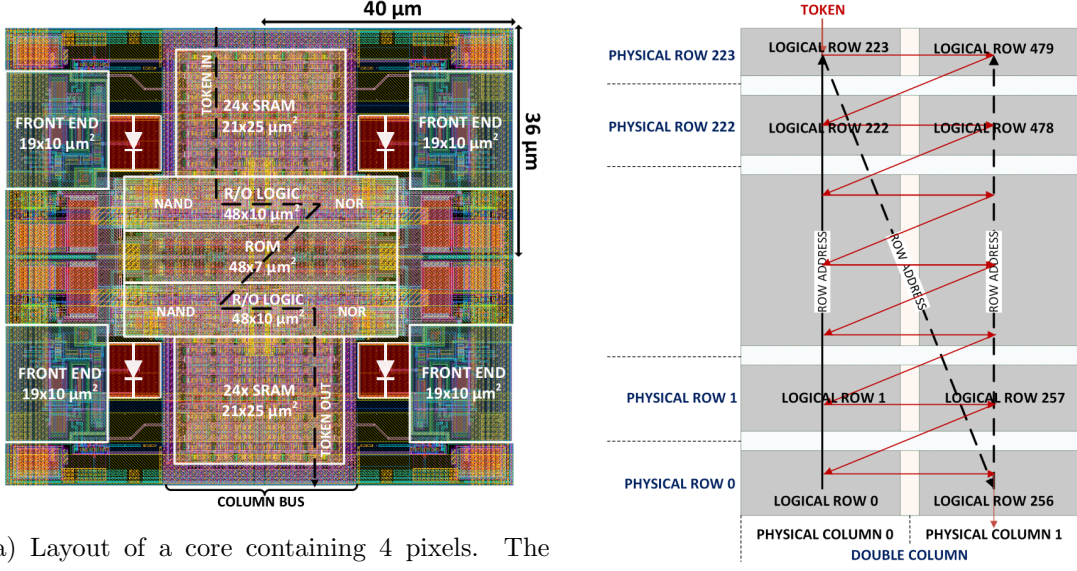
716 The TJ-Monopix1 chip contains, apart from the pixels matrix, all the required support
 717 blocks used for configuration and testing:

- 718 • the whole matrix contains 224×448 pixels, yielding a total active area approximately
 719 equal to 145 mm^2 over a total area of $1 \times 2 \text{ cm}^2$;
- 720 • at the chip periphery are placed some 7-bit Digital to Analog Converter (DAC), used
 721 to generate the analog bias voltage and current levels and to configugre the FE;
- 722 • at the EoC is placed a serializer to transferred datas immediately, indeed no trigger
 723 memory is implemented in this prototypes;
- 724 • the matrix power pads are distributed at the sides
- 725 • four pixels which have analog output and which can be monitored with an oscillo-
 726 scope, and therefore used for testing

727 Pixels are grouped in 2×2 cores (fig. 4.2a): this layout allows to separate the analog
 728 and the digital electronics area in order to reduce the possible interference between the
 729 two parts. In addition it semplifies the routing of data as pixels on double column share
 730 the same column-bus to EoC. Therefore pixels can be addressed through the physical
 731 column/row or through the logical column/row, as shown in fig. 4.2b: in figure is also
 732 highlighted the token propagaion path, whose I will discuss later.

733 4.1 The sensor

734 As already anticipated, TJ-Monopix1 has a p-type epitaxial layer and a n doped small
 735 collection electrode ($2 \mu\text{m}$ in diameter); to avoid the n-wells housing the PMOS transistors
 736 competing for the charge collection, a deep p-well substrate, common to all the pixel FE
 737 area, is used. TJ-Monopix1 adopts the modification described in section 2.4.2 that allows
 738 to achieve a planar depletion region near the electrode applying a relatively small reverse
 739 bias voltage. This modification improves the efficiency of the detector, especially after
 740 irradiation, however a simulation of the electric field in the sensor, made with the software
 741 TCAD (Technology Computer Aided Design), shows that a nonuniform field is still pro-
 742 duced in the lateral regions of the pixel compromising the efficiency at the corner. Two



(a) Layout of a core containing 4 pixels. The analog FE and the digital part are separated in order to reduce cross-talk be

(b)

Parameter	Value
Matrix size	$1 \times 2 \text{ cm}^2$
Pixel size	$36 \times 40 \mu\text{m}^2$
Depth	$25 \mu\text{m}$
Electrode size	$2 \mu\text{m}$
BCID	40 MHz
ToT-bit	6
Power consumption	$\sim 120 \text{ mW/cm}^2$

Table 4.2

variations to the process have been proposed in order to further enhance the transversal component of electric field at the pixel borders: on a sample of chip, which includes the one in Pisa, a portion of low dose implant has been removed, creating a step discontinuity in the deep p-well corner (fig. 4.3); the second solution proposed[MOUSTAKAS THESY, PAG 58] consists in adding an extra deep p-well near the pixel edge. A side effect of the alteration in the low dose implant is that the separation between the deep p-well and the p-substrate becomes weak to the point that they cannot be biased separately to prevent the punchthrough.

Moreover, to investigate the charge collection properties, pixels within the matrix are split between bottom top half and bottom half and feature a variation in the coverage of the deep p-well: the electronics area can be fully covered or not. In particular the pixels belonging to rows from 0 to 111 are fully covered (FDPW) and pixels belonging to rows from 112 to 223 have a reduced p-well (RDPW), resulting in a enhancement of the lateral component of the electric field.

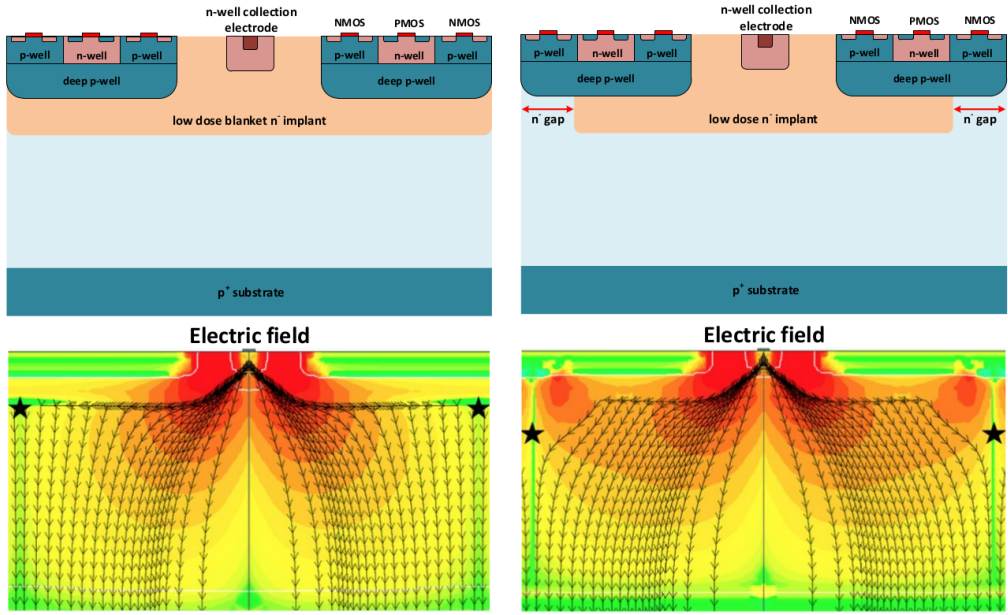


Figure 4.3: (a) The cross-section of a monolithic pixel in the TJ-Monopix with modified process; additionally in (b) a gap in the low dose implant is created to improve the collection of charge due to a bigger lateral component of the electric field. this point in figure is indicated by a star . transversal component of the electric field drops at the pixel corner

757 4.2 Front end

758 The matrix is split in four sections, each one corresponding to a different flavor of the FE.
 759 The four variation have been implemented in order to test the data-bus readout circuits
 and the input reset modes.

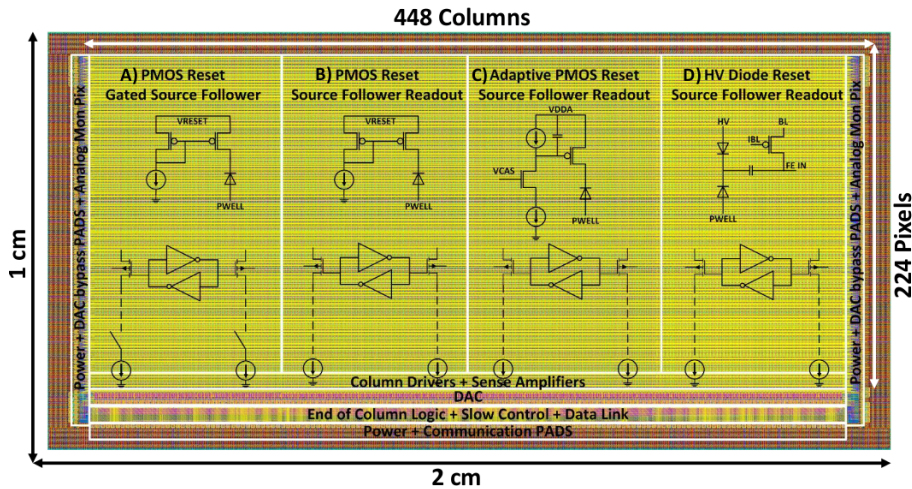


Figure 4.4

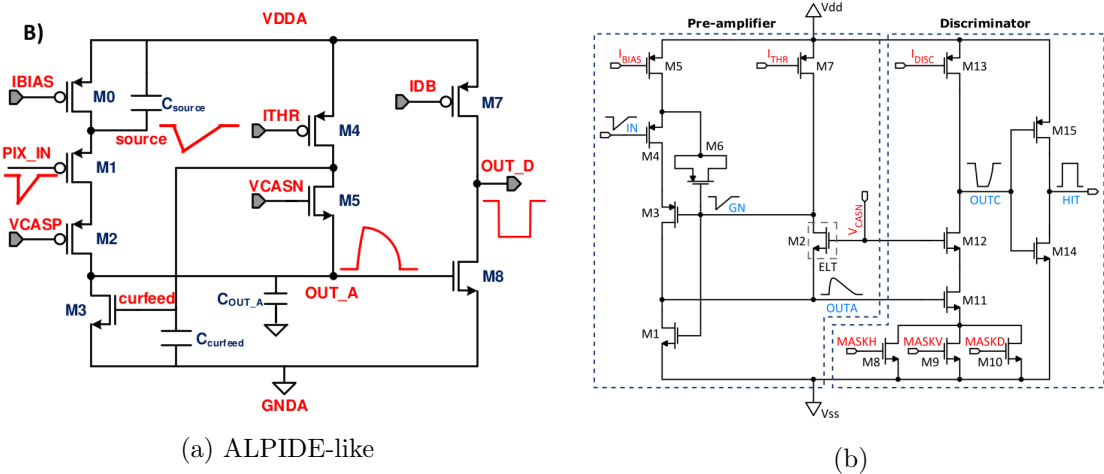
760 All the flavors implement a source-follower double-column bus readout: the standard
 761 variation is the flavor B, that features a PMOS input reset (refered as "PMOS reset").
 762 Flavor A is identical to flavor B except for the realization of the source follower (it is a
 763 gated one) that aim to reduce the power consumption.
 764 cosa significa? C instead implements

765 a novel leakage compensation circuit. Moreover the collection electrode in flavors A, B, C
 766 is DC-coupled to the front-end input, while in D is AC-coupled, providing to applu a high
 767 bias voltage; for this reason flavor D il called "HV flavor".

768 Principio generale: R resistenza di reset deve essere abbastanza grande in modo da
 769 far si che il ritorno allo zero è abbastanza lento (non devi "interferire" con la tot slope e
 770 non deve essere più corto del tempo del preamplificatore, sennò hai perdita di segnale).
 771 Baseline reset: all'input solitamente hai un PMOSS o un diodo; R reset

772 4.2.1 ALPIDE-like

773 ALPIDE chips, developed by the ALICE collaboration, implemented a standard FE to the
 774 point that many CMOS MAPS detectors used a similar FE and are called "ALIPDE-like".
 775 Considering that both TJ-Monopix1 and ARCADIA-MD1 have an ALPIDE-like FE, I am
 going to explain the broad principles of the early FE stage. The general idea is of the



776
 777 amplification to transfer the charge from a bigger capacity[14], C_{source} , to a smaller one,
 778 C_{out} : the input transistor M1 with current source IBIAS acts as a source follower and this
 779 forces the source of M1 to be equal to the gate input $\Delta V_{PIX_IN} = Q_{IN}/C_{IN}$.

$$Q_{source} = C_{source} \Delta V_{PIX_IN} \quad (4.1)$$

780 The current in M2 and the charge accumulates on C_{out} is fixed by the one on C_{source} :

$$\Delta V_{OUT_A} = \frac{Q_{source}}{C_{OUT_A}} = \frac{C_{source} \Delta V_{PIX_IN}}{C_{OUT_A}} = \frac{C_{Source}}{C_{OUT_A}} \frac{Q_{IN}}{C_{IN}} \quad (4.2)$$

781 A second branch (M4, M5) is used to generate a low frequency feedback, where VCASN
 782 and ITHR set the baseline value of the signal on C_{OUT_A} and the velocity to goes down
 783 to the baseline.

784 IL RUOLO DI CURVFEED NON L'HO CAPITO.

785 Finally IDB defines the charge threshold with which the signal OUT_A must be compared:
 786 depending on if the signal is higher than the threshold or not, the OUT_D is high or low
 787 respectively.

788 The actual circuit implemented in TJ-Monopix1 is shown in figure 4.5b: the principal
 789 difference lays in the addition of disableing pixels' readout. This possibility is uttermost
 790 important in order to reduce the hit rate and to avoid saturating the bandwidth due to the

Parameter	Meaning	
IBIAS	mainly controls the rise time	yes? check
IDB	sets the discriminator threshold	yes
ITHR	sets the velocity of the return to the baseline	yes
ICASN	sets the baseline of the signal	yes
VRESET	sets the gain of the preamplifier	yes
IRESET	sets the gain of the preamplifier	no

Table 4.3: FE parameters which must be setted through the DAQ. "Function" means that higher parameter implies higher value

791 noisy pixels, which typically are those with manufacturing defects. In the circuit transis-
 792 tors M8, M9 and M10 have the function of disabling registers with coordinates MASKH,
 793 MASKV and MASKD (respectively vertical, orizontal and diagonal) from readout: if all
 794 three transistors-signals are low, the pixel's discriminator is disabled. Compared with a
 795 configurable masking register which would allow disableing pixels individually, to use a
 796 triple redundancy reduces the sensistivity to SEU but also gives amount of intentionally
 797 masked ("ghost") pixels. This approach is suitable only for extremely small number N of
 798 pixel has to be masked: if two coordinate projection scheme had been implemented, the
 799 number of ghost pixels would have scale with N^2 , if instead three coordinates are used,
 the N's exponential is lower than 2 (fig. 4.6)

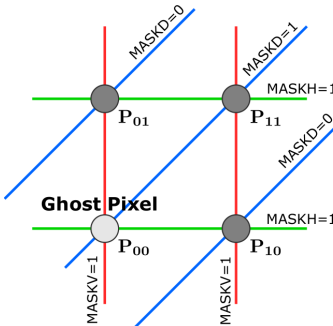


Figure 4.6

800

801 4.3 Readout logic

802 TJ-Monopix1 has a triggerless, fast and with ToT capability R/O which is based on a
 803 column-drain architecture. On the pixel are located two Random Access Memory (RAM)
 804 cells to store the 6-bit LE and 6-bit TE of the pulse, and a Read-Only Memory (ROM)
 805 containing the 9-bit pixel address. Excluded these memories, TJ-Monopix1 hasn't any
 806 other buffer: if a hit arrives while the pixel is already storing a previous one, the new
 807 data get lost. After being read, the data packet is sent to the EoC periphery of the
 808 matrix, where a serializer transfers it off-chip to an FPGA (4.7). There a FIFO is used
 809 to temporarily stored the data, which is transmitted to a computer through an ethernet
 810 cable in a later time.

811 The access to the pixels' memory and the transmission of the data to the EoC, following

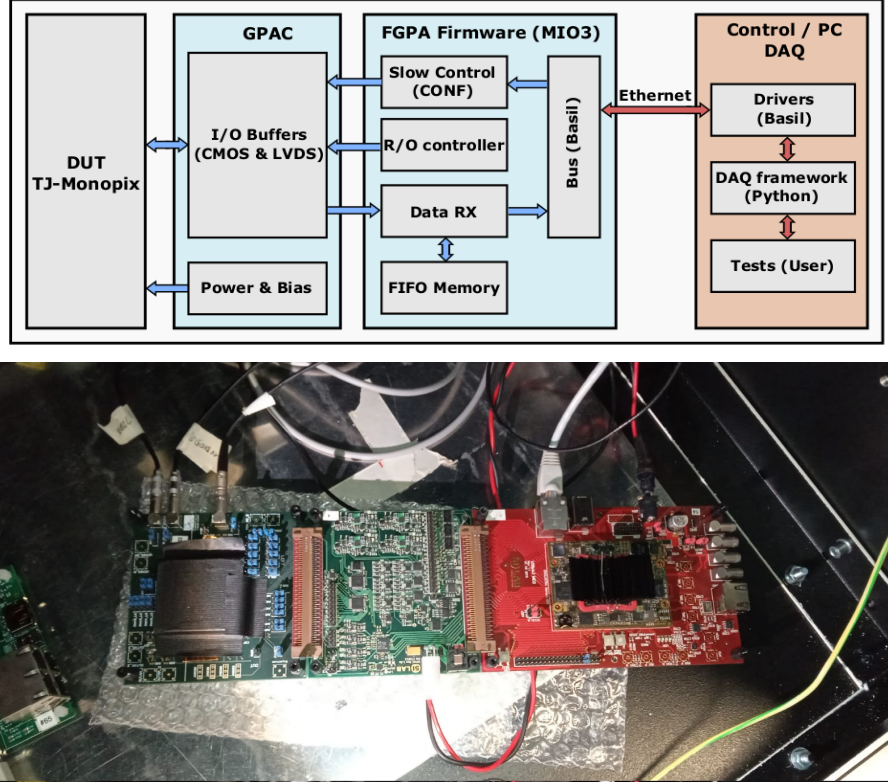
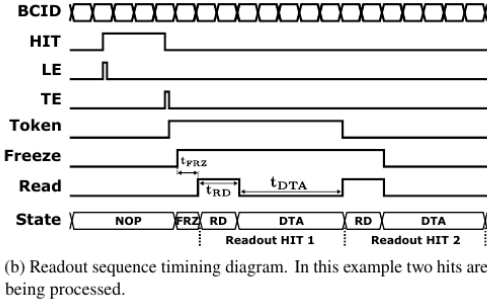


Figure 4.7: Main caption

a priority chain, is managed by control signals and is based on a Finite State Machine (FSM) composed by four state: no-operation (NOP), freeze (FRZ), read (RD) and data transfer (DTA). The readout sequence (??) starts with the TE of a pulse: the pixel immediately tries to grab the column-bus turning up a hit flag signal called *token*. The token is used to control the priority chain and propagates across the column indicating what pixel that must be read. To start the readout and avoid that the arrival of new hits disrupt the priority logic, a *freeze* signal is activated, and then a *read* signal controls the readout and the access to memory. During the freeze, the state of the token for all pixels on the matrix remains settled: this does not forbid new hits on other pixels from being recorded, but forbids pixels hit from turning on the token until the freeze is ended. The freeze stays on until the token covers the whole priority chain and gets the EoC: during that time new token cannot be turned on, and all hits arrived during a freeze will turn on their token at the end of the previous freeze. Since the start of the token is used to assign a timestamp to the hit, the token time has a direct impact on the time resolution measurement; this could be a problem coping with high hits rate.

The analog FE circuit and the pixel control logic are connected by an edge detector which is used to determine the LE and the TE of the hit pulse(fig. 4.9): when the TE is stored in the first latch the edge detector is disabled and, if the **FREEZE** signal is not set yet, the readout starts. At this point the HIT flag is set in a second latch and a token signal is produced and depending on the value of **Token in** the pixel can be read or must wait until the **Token in** is off. In figure an OR is used to manage the token propagation, but since a native OR logic port cannot be implemented with CMOS logic, a sum of a NOR and of an inverter is actually used; this construct significantly increases the propagation



(b) Readout sequence timing diagram. In this example two hits are being processed.

Figure 4.8: Readout timing diagram: in this example two hits are being processed

835 delay (the timing dispersion along a column of 0.1-0.2 ns) of the token and to speed up
 836 the circuit optimized solution are often implemented. When the pixel become the next to
 837 be read in the queue, and at the rising edge of the **READ** signal, the state of the pixel is
 838 stored in a D-latch and the pixel is allowed to use the data bus; the TE and the HIT flag
 839 latches are reset and a **READINT** signal that enable access of the RAM and ROM cells
 840 is produced.

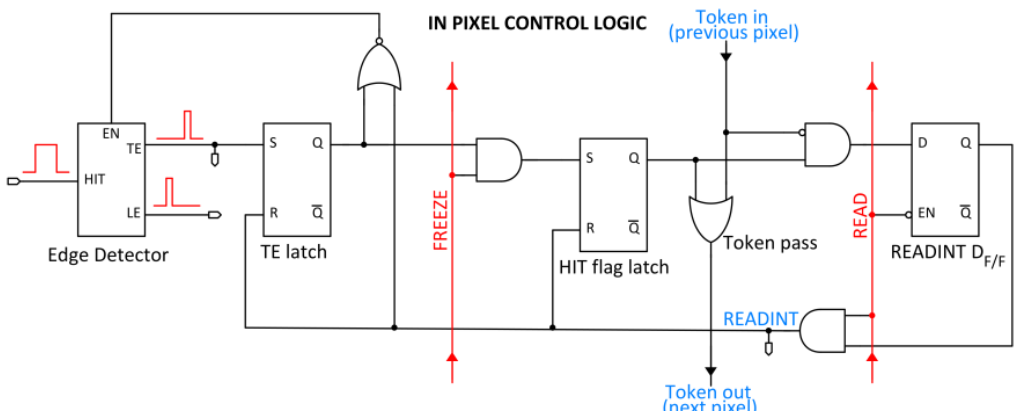


Figure 4.9

841
 842 The final data must provide all the hits' information: the pixel address, the ToT and
 843 the timestamp. All those parts are assigned and appended at different time during the
 844 R/O chain:

- 845 • **Pixel address:** while the double column address (6-bit) is appended by the EoC
 846 circuit, the row address (8-bits for each flavor) and the physical column in the doublet
 847 (1-bit) are assigned by the in-pixel logic
- 848 • **ToT:** is obtained offline from the difference of 6-bits TE and 6-bits LE, stored by
 849 the edge detector in-pixel; since a 40 MHz BCID is distributed across the matrix,
 850 the ToT value is range 0-64 clock cycle which corresponds to 0-1.6 μ s
- 851 • **Timestamp:** The timestamp of the hit correspond to the time when the pixel set
 852 up the token; it is assigned by the FPGA, that uses the LE, TE and a 640 MHz
 853 clock to derive it. For all those hits which arrived while the matrix is frozen, the
 854 timestamp is no more correlated with the time of arrival of the particle

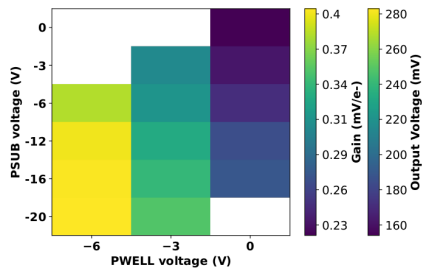


Figure 4.10: 2D map of the output voltage amplitude and gain with respect to the p-well and p-substrate in the case of the PMOS reset front-end

855 When the bits are joined up together the complete hit data packet is 27-bit.

856 Measurement of the magnitude of the collected charge has also been generally available
 857 for pixel detectors, and has been used to improve the 3D space point precision through
 858 interpolation as well as for particle identification through specific ionization measurement.

859 **Chapter 5**

860 **Arcadia-MD1**

861 [15] [16]

862 Breve introduzione analoga a Monopix1 in cui descrivo brevemente la "timeline" da
863 SEED Matisse a Md1 e Md2

864 **5.1 The sensor**

865 ARCADIA-MD1 is an LFoundry chip which implements the technology 110 nm CMOSS
866 node with six metal layer ???. The standard p-type substrate was replaced with an n-type
867 floating zone material, that is a tecnique to produce purified silicon crystal. (pag 299
868 K.W.).

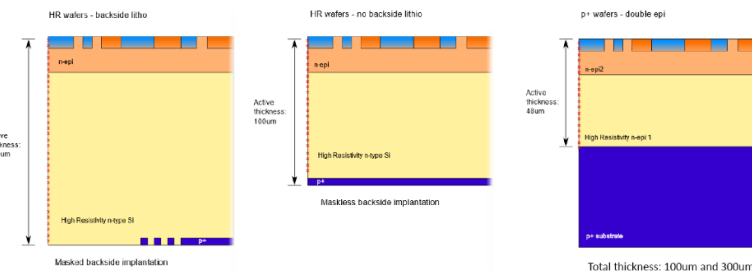


Figure 5.1

869
870 Wafer thinning and backside lithography were necessary to introduce a junction at the
871 bottom surface, used to bias the substrate to full depletion while maintaining a low voltage
872 at the front side.

873 C'è un deep pwell per - priority chainseparare l'elettronica dal sensore; per controllare il
874 punchthrough è stato aggiunto un n doped epitaxial layer having a resistivity lower than
875 the substrate.

876 RILEGGI SUL KOLANOSKY COS'È IL PUNCHTHROUGH, FLOAT ZONE MA-
877 TERIAL, COME VENGONO FATTI I MAPS COME FAI LE GIUNZIONI

878 It is part of the cathegory of DMAPS Small electrode to enhance the signal to noise
879 ratio.

880 It is operated in full depletion with fast charge collection by drift.

881 Prima SEED si occupa di studiare le prestazioni: oncept study with small-scale test

882 structure (SEED), dopo arcadia: technology demonstration with large area sensors Small
 883 scale demo SEED(sensor with embedded electronic developement) Quanto spazio dato
 884 all'elettronica sopra il pwell e quanto al diodo. ..

885 5.2 Readout logic and data structure

886 5.2.1 Matrix division and data-packets

887 The matrix is divided into an internal physical and logical hierarchy: The 512 columns are
 888 divided in 16 section: each section has different voltage-bias + serializzatori. Each section
 889 is devided in cores () in modo che in ogni doppia colonna ci siano 1Pacchetto dei dati 6
 890 cores. ricordati dei serializzaatori: sono 16 ma possono essere ridotti ad uno in modalità
 spazio

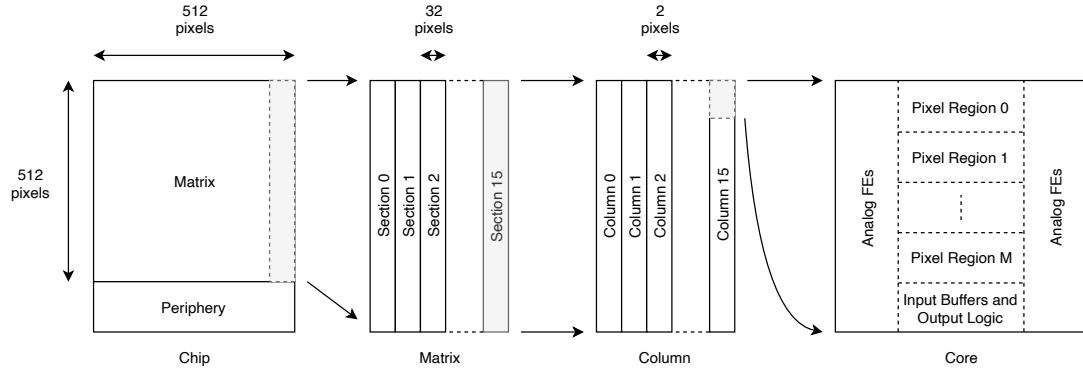


Figure 5.2

891

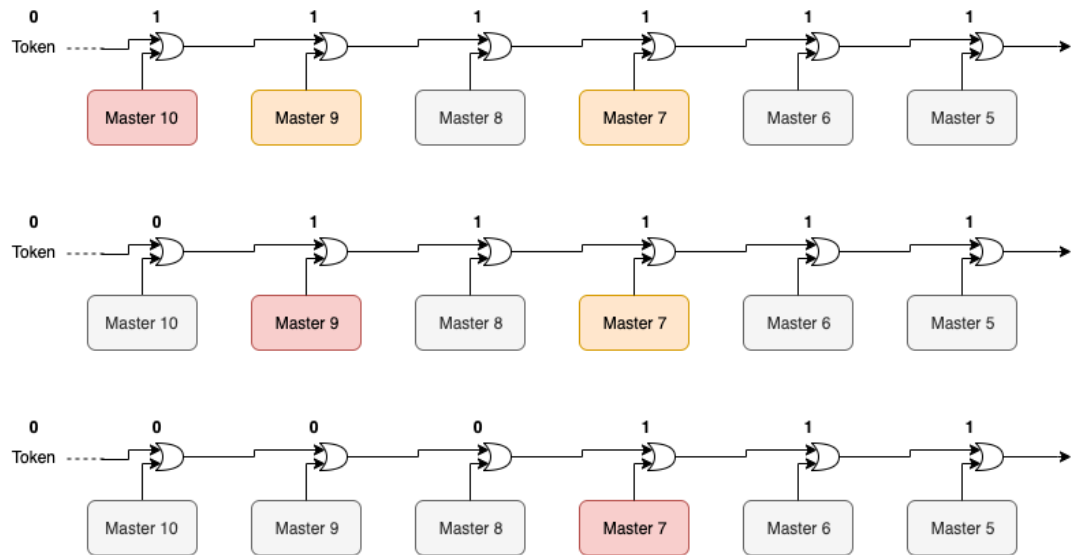


Figure 5.3

892 Questa divisione si rispecchia in come sono fatti i dati: scrivi da quanti bit un dato è
 893 fatto e le varie coordinate che ci si trovano dentro; devi dire che c'è un pixel hot e spieghi
 894 dopo a cosa serve, e devi accennare al timestamp

895 "A core is simply the smallest stepped and repeated instance of digital circuitry. A
 896 relatively large core allows one to take full advantage of digital synthesis tools to imple-

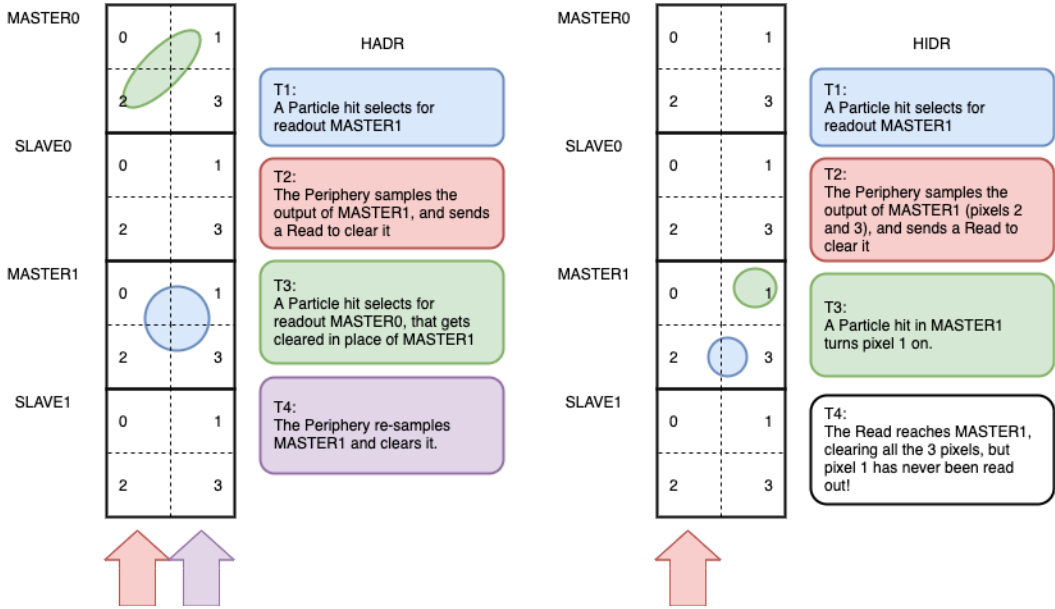


Figure 5.4

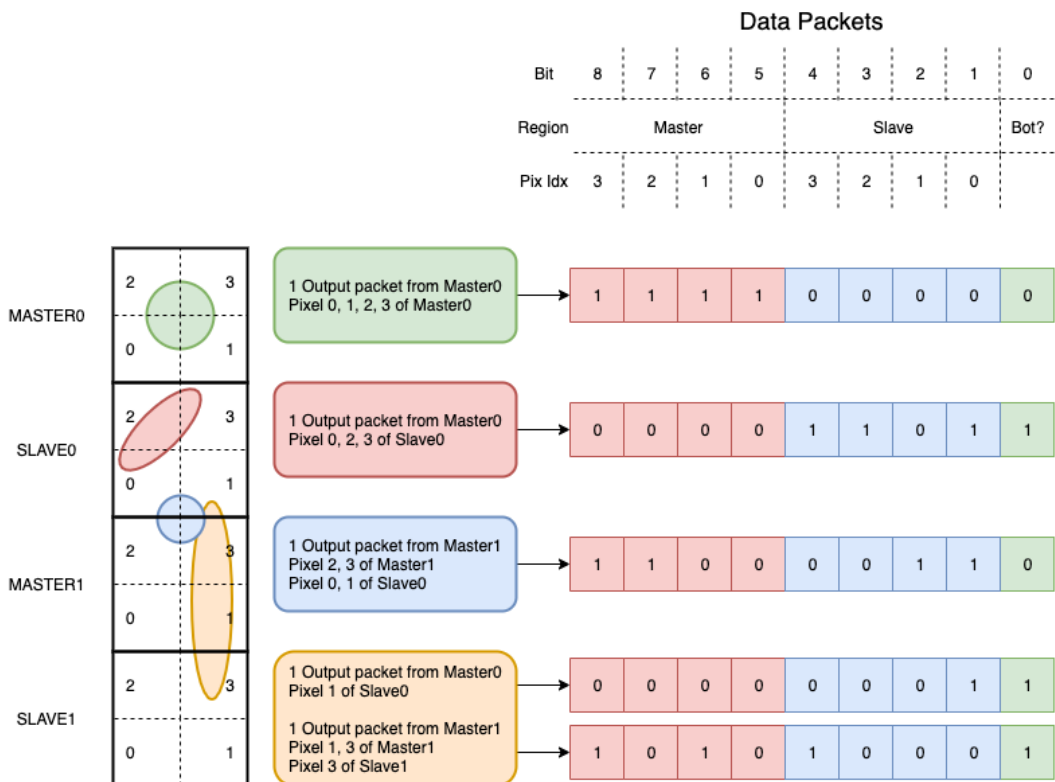


Figure 5.5

ment complex functionality in the pixel matrix, sharing resources among many pixels as needed.”. pagina 28 della review.

899

900 TABELLA: con la gerarchia del chip Matrix (512x512 pixels) Section (512x32 pixels)
901 Column (512x2) Core (32x2) Region (4x2)

902 Nel chip trovi diverse padframe: cosa c’è nelle padframe e End of section.

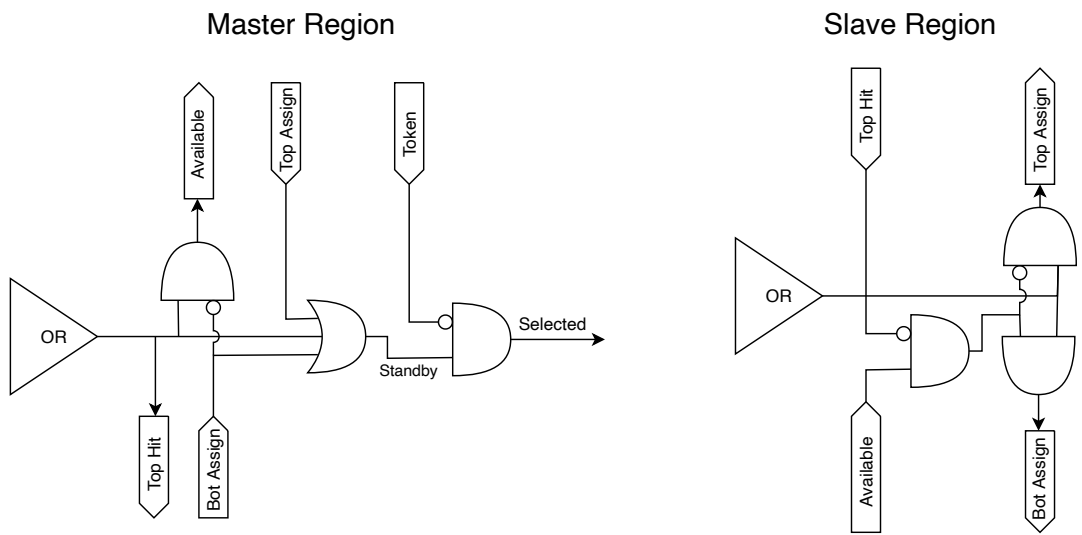


Figure 5.6

903 "DC-balance avoids low frequencies by guaranteeing at least one transition every n
 904 bits; for example 8b10b encoding n =5"

905 **Chapter 6**

906 **Characterization**

907 rifai il conto della lunghezza di attenuazione. Ho trovato (presentazione Luciano Mus) 29
908 um per ka e 37 um per kb.

909 **6.1 TJ-Monopix1 characterization**

910 **6.1.1 Threshold and noise: figure of merit for pixel detectors**

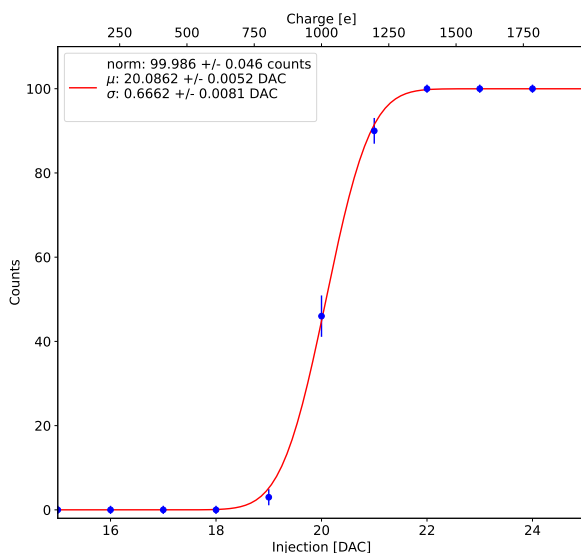


Figure 6.1: S-curve for pixel (10, 10) of the PMOS flavor (flavor 1) with IDB fixed at 40 DAC. The conversion of charge injected from DAC to electrons has been done assuming a conversion factor of 20 e⁻/DAC.

911 A characterization of threshold and noise is typically necessary since these values have
912 an impact on the operating conditions and on the performance of the chips. infact, the
913 signal to threshold ratio may be considered as the figure of merit for pixel detectors rather
914 than the signal to noise ratio. The mean minimum stable threshold evolved through
915 different generation of chips: in the 1st generation it was around 2500 e⁻ while in the
916 3rd (corresponding to nowadays chips) is less than 500 e⁻. This allows in thinner sensors
917 with smaller signals: from 16 000 e⁻ produced in 200 μ m, the signal expected moved down

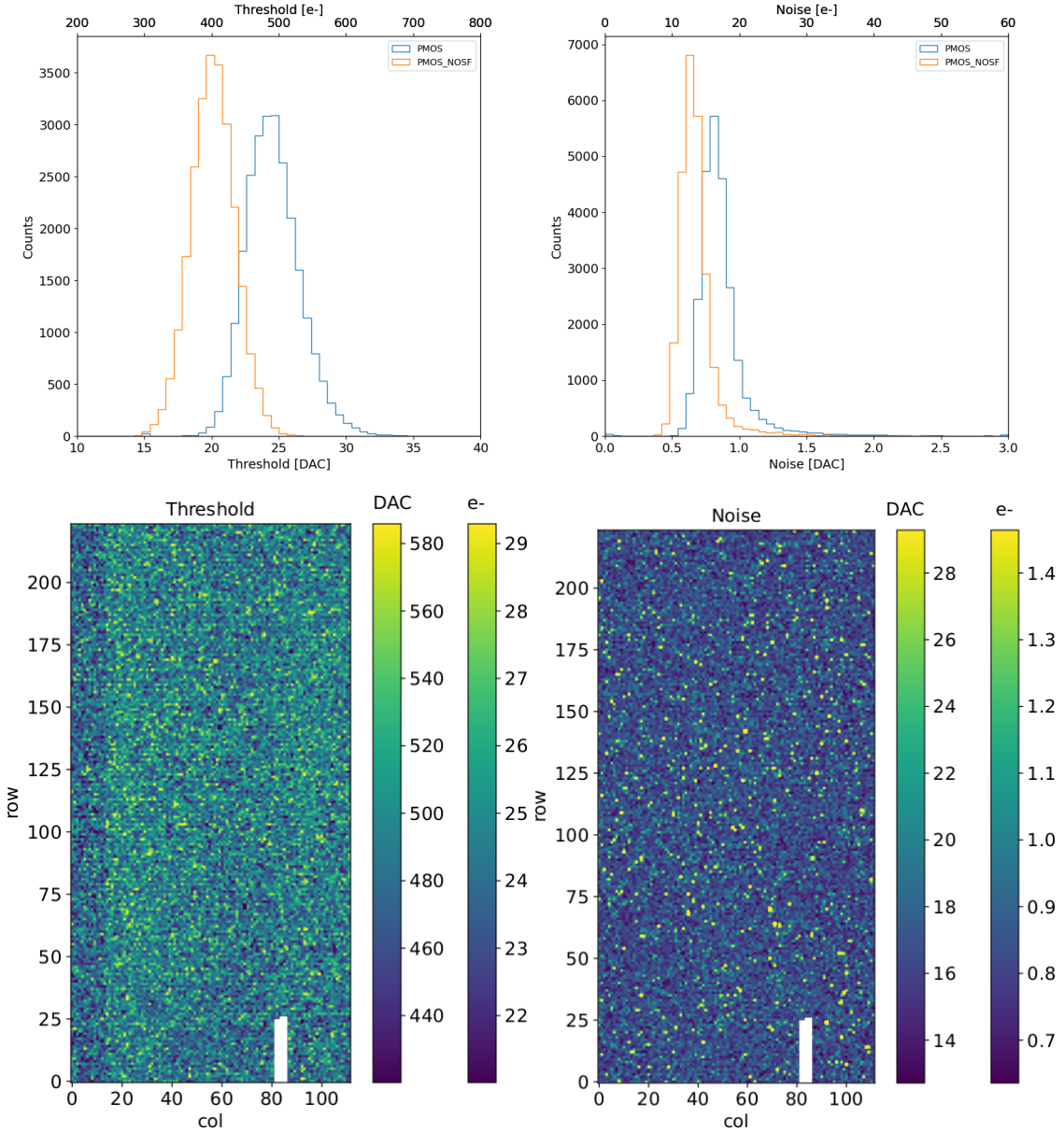


Figure 6.2: Histograms of the threshold (a) and the noise (b) found fitting the s-curve of all flavor with IDB fixed at 40 DAC. Maps of the threshold (a) and the noise (b) found fitting the s-curve with IDB fixed at 40 DAC. The white pixels have the injection circuit broken.

918 to 2000 e⁻ produced in 25 μm. According with this ??, the threshold of TJ-Monopix1 is
 919 around 500 e⁻. The following prototypes have lower threshold and noise, for example TJ-
 920 Monopix2 has check, according to the above. The threshold has to be located between the
 921 noise peak around the baseline and the signal distribution, in particular it has to be low
 922 enough to mantain a high signal efficiency, but also high enough to cut the noise: for a low
 923 threshold many pixels can fire at the same time and a positive feedback can set off a chain
 924 reaction eventually, causing all the other pixels to fire. Thus, the noise sets a lower bound
 925 to the threshold: if an occupancy $\leq 10^{-4}$ is required, for example, this correspond to the
 926 Gaussian 1-sided tail fraction for 3.7σ . In this case, if the noise is 100 e⁻, for example, the
 927 threshold must be higher than 3.7×100 e⁻. Typically this argument sets only a minimal

928 bound to the threshold since the variation with time and from pixel to pixel have to be
 929 taken into account: the temperature, the annealing (for example, the radiation damages in
 930 the oxide layer causes shift of MOSFET threshold voltage) and the process parameters
 931 variation across the wafer (as for example process mismatch between transistors).

932 On the other hand the noise is valued at the preamplifier input node given that the
 933 first stage of amplification is the most crucial since the signal amplitude is high compared
 934 to additional noise introduced by the following stages. The noise is then parameterized as
 935 Equivalent Noise Charge (ENC), which is defined as the ratio between the noise N at the
 936 output expressed in Volt and the out voltage signal S produced by $1e^-$ entering in the
 937 preamplifier:

$$ENC = \frac{N_{out}[V]}{S_{out}[V/e^-]} = \frac{V_{noise}^{RMS}}{G} \quad (6.1)$$

938 with G expressed in V/e $^-$; as the gain increases, the noise reduces .

939 **ENC is mainly influenced by the total input capacitance and by the system band-**
 940 **width: if the bandwidth is constant, noise can be reduced by increasing the input transis-**
 941 **tor transconductance (and consequently power consumption).** Considering the threshold
 942 dispersion a requirement for the ENC is:

$$ENC < \sqrt{(T/3.7)^2 - T_{RMS}^2(x) - T_{RMS}^2(t)} \quad (6.2)$$

943 where the T is the threshold set, T_{RMS} is the threshold variation during time (t) and
 944 across the matrix (x); a typical reasonable value often chosen is 5 ENC.

945 Because of the changing of the 'real' threshold, the possibility of changing and adapting
 946 the setting parameters of the FE, both in time and in space is desiderable: these parameters
 947 are usually set by Digital to Analog Converter (DAC) with a number of bit in a typical
 948 range of 3-7. Unfortunately DAC elements require a lot of space that may be not enough
 949 on the pixel area; therefore, the FE parameters are typically global, which means that they
 950 are assigned for the whole chip, or they can be assigned for regions the matrix is divided
 951 into. The former case corresponds to TJ-Monopix1's design in which 7 bits are used for
 952 a total 127-DAC possible values, while the latter corresponds to the ARCADIA-MD1's
 953 one, **where quanti bit??**. An other possibility, for example implemented in TJ-Monopix2,
 954 is allocate the space on each pixel for a subset of bits, then combinig the global threshold
 955 with a fine tuning. If so, the threshold dispersion after tuning is expected to be inversely
 956 proportional to the tuning DAC number of bits and thus be improved a lot:

$$\sigma_{THR,tuned} = \frac{\sigma_{THR}}{2^{nbit}} \quad (6.3)$$

957 where σ_{thr} is the RMS of the threshold spread before tuning.

958 To measure the threshold and noise of pixels a possible way is to make a scan with
 959 different known injected charge: the threshold corresponds to the value where the efficiency
 960 of the signal exceeds the 50%, and the ENC is determined from the width of this edge.
 961 Following this path, I have used the injection circuit available on the chip to inject 100
 962 pulses for each input charge for a fixed threshold. The injection comes on a capacity at the
 963 input of the FE circuit, whose mean value is 230 aF and from which the conversion factor
 964 from DAC units to electrons can be obtained: for the PMOS flavor, for example, since
 965 the DAC are biased at 1.8 V, the Least significant Bit (LSB) corresponds to a voltage of
 966 14.7 mV from which the charge for LSB $1.43e^-/mV$ and the conversion factor therefore
 967 is $20.3e^-/\text{DAC}$. While this value is equivalent for all the PMOS flavor, the HV flavor

	DAC units	electrons
Threshold	24.529 ± 0.049 u: 24.433 ± 0.049 d: 24.623 ± 0.051	
Threshold dispersion	1.848 ± 0.033 u: 1.867 ± 0.034 d: 1.825 ± 0.035	
Noise	0.8222 ± 0.0043 u: 0.8225 ± 0.0045 d: 0.8221 ± 0.0043	
Noise dispersion	0.0975 ± 0.0030 u: 0.0968 ± 0.0031 d: 0.0970 ± 0.0030	

Table 6.1: Flavor PMOS, IDB fixed at 40 DAC

968 is expected to have a different conversion factor, $\sim 33 \text{ e-}/\text{DAC}$, because of the different
 969 input capacity.

970 Besides the charge, also the duration and the period of the injection pulse can be set;
 971 it is important to make the duration short enough to have the falling edge during the dead
 972 time of the pixel (in particular during the FREEZE signal) in order to avoid the undershoot,
 973 coming at high input charge, triggering the readout and reading spurious hits. Since the injection circuit is coupled in AC to the FE, if the falling edge of the pulse
 974 is sharp enough to produce an undershoot, this can be seen as a signal.

975 Assuming a gaussian noise, the efficiency of detecting the signal can be described
 976 through a modification of the error function:

$$f(x, \mu, \sigma) = \frac{1}{2} \left(1 + \operatorname{erf} \left(\frac{x - \mu}{\sigma\sqrt{2}} \right) \right) \quad (6.4)$$

977 with: where the threshold and the ENC corresponds to the μ and σ . Therefore I perform
 978 a fit of the counts detected using the function in equation 6.4. In figure 6.1 there is an
 979 example with IDB (look at table 6.1 for the meaning of the parameter) equal to 40 DAC
 980 of fit for a pixel belonging to the flavor 1, while in table 6.1 and figure ?? and ?? there
 981 are the histograms and the maps of the parameters of the scurve-fit.

982 To verify the trend of the threshold as a function of the front end parameter IDB, I
 983 have performed a scan with different IDBs: I have injected the whole matrix and found
 984 the means and the standard deviation of the distributions. The results are shown in figure
 985 6.3.

986 6.1.2 Linearity of the ToT

987 I have already said in chapter 4 that TJ-Monopix1 returns an output signal proportional to
 988 the charge released by a particle in the epitaxial layer, which is the Time over Threshold;
 989 the ToT is saved as a 6-bit variable and then has a dynamic range equal to 0-64, which
 990 corresponds to $0 \mu\text{s}$ to $1.6 \mu\text{s}$ assuming a clock frequency of 40 MHz. When a pulse is longer
 991 than $1.6 \mu\text{s}$ the counter rolls back to zero and there is no way to distinguish that charge
 992 from a lower one with the same ToT: that is the rollover of the ToT (??(a)).

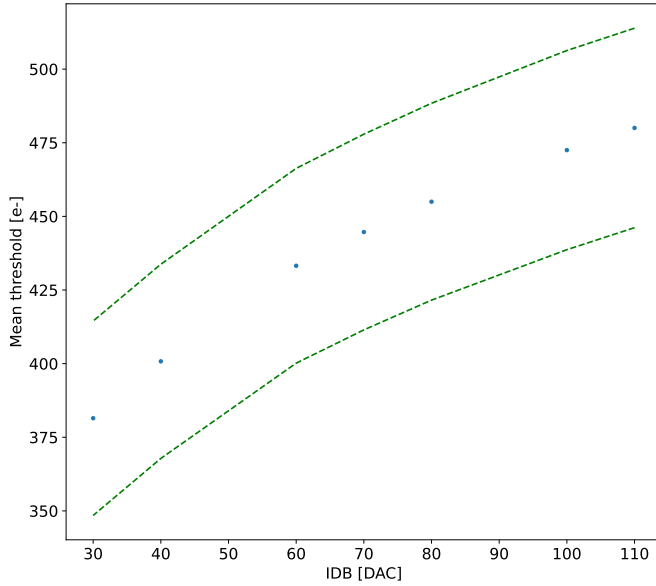


Figure 6.3

994 In order to associate the ToT (in range 0-64) to the charge, a calibration of the signal
 995 is necessary. Assuming the linearity between ToT and the charge, Q can be found:

$$Q [DAC] = \frac{(ToT [au] - q [au])}{m [au/DAC]} \quad (6.5)$$

996 where m and q are the fitted parameters of the calibration. It is important to keep in
 997 mind that the main application target of TJ-Monopix1 is in the inner tracker detector of
 998 HEP experiments, then the main feature is the efficiency, then a rough calibration of the
 999 signal to charge is fine; **this information can be used to improve??.**

1000 The study of the output signal is made possibile via the injection: since the pulses
 1001 are triangular, the ToT is expected to be almost linear depending on the injection charge
 1002 value. To verify this statement and study the deviations from linearity I've fit the ToT
 1003 versus the charge injected for all pixel within the matrix. In figure ??(b) there is an
 1004 example of fit for a pixel belonging to the flavor 1, while in figure 6.5 and ?? there are the
 1005 histograms and the maps of the parameters of the line-fit for all flavors with IDB fixed at
 1006 40 DAC.

1007 Before performing the fit I have calculated the mean value of the ToT of the pulses
 1008 recorded for each pulse amplitude and I used the mean ToT as value for the fit. The aim
 1009 of the calibration obviously is finding a relation only in the range 0-64 without taking into
 1010 account the rolling over hits: therefore, to prevent the rollover data from reducing the
 1011 mean ToT introducing a bias in the mean value, I cut and I did not consider them. If a
 1012 signal bigger than the 1.6 μ s is expected in the usage of the detector, the threshold must be
 1013 raised or the gain reduced, making the expected output signal in range 0-64. In figure ??
 1014 (b) are shown both the fits with a line (red) and with a second order polynomial (green):
 1015 at the bounds of the ToT range values deviate from the line model. Since the deviation is
 1016 low than **controlla quant'era, questo ha un impatto sul valore della calibrazione di tipo ..**

	PMOS 0	PMOS 1	PMOS 2	HV
Slope [au/DAC]	0.75566 ± 0.00149	0.57145 ± 0.00025		
Slope dispersion [au/DAC]	0.03841 ± 0.00037	0.01685 ± 0.00016		
Intercept [au]	-11.6070 ± 0.0089	-10.824 ± 0.019		
Intercept dispersion [au]	1.5176 ± 0.0063	1.225 ± 0.013		

Table 6.2: Mean calibration parameters for all flavor and their dispersion on the matrix.

1017 che è trascurabile al primo ordine. e comunque hai problemi ai bounds mentre al centro
 1018 hai comunque una buona linearità.. Chiarire la differenze negli istogrammi e come mai ci
 1019 sono delle bande nelle mappe.

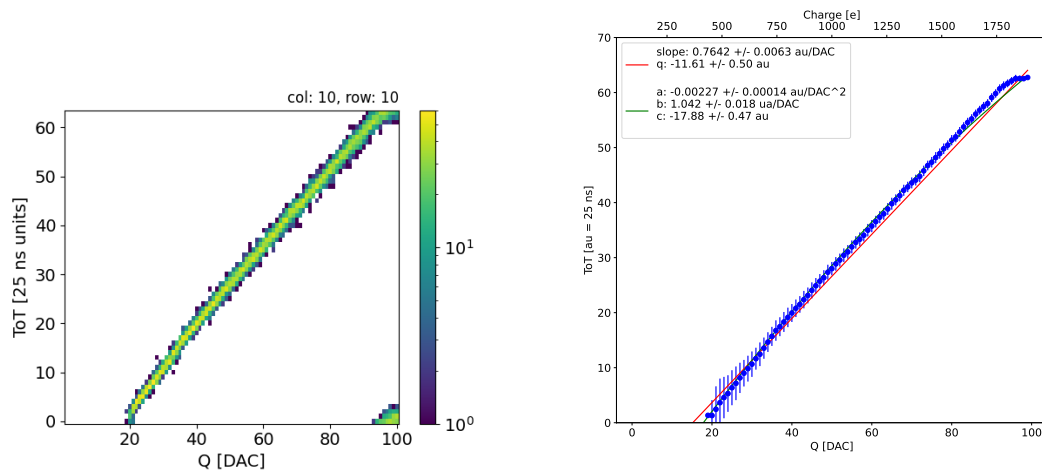


Figure 6.4: The figures refer to pixel (10,10) of the PMOS-reset flavor (1) with IDB fixed at 40 DAC. (a) Histogram of the injection pulses: the ToT is in range 0-64 since it is represented by 6 bit, so when achieving the 64 it rolls over back to the zero. (b) Mean ToT vs the the charge: the mean has been calculated cutted the rolling hits.

1020 perchè noise e th sono diverse per diversi flavor? Controlla cos' hanno di diverso.

1021 6.1.3 Calibration of the ToT

1022 Considering that the charge injected in the FE goes to fill capacitor which is different from
 1023 pixel to pixel, the true charge injected does not correspond to what expected assuming C
 1024 equal to 230 aF, the nominal value. Accordingly to that, a verification of the value provided
 1025 and an absolute calibration of this capacity and of the conversion factor F is needed to
 1026 have a correspondence of the signal in electrons; assuming C 230 aF, F is expected to be
 1027 20 e-/DAC, and is defined as:

$$F [e^- / DAC] = \frac{1616 e^-}{Q [DAC]} \quad (6.6)$$

1028 For this purpose a Fe55 radioactive source has been employed; the Fe55 is an extremely
 1029 important radionuclide in the calibration of X-ray spectrometers, proportional counter
 1030 and scintillator detector since it emits two X-photons during the electron capture
 1031 decay: the first one (K_α) at 5.9 keV and the second one (K_β) at 6.5 keV. The K_α photon,

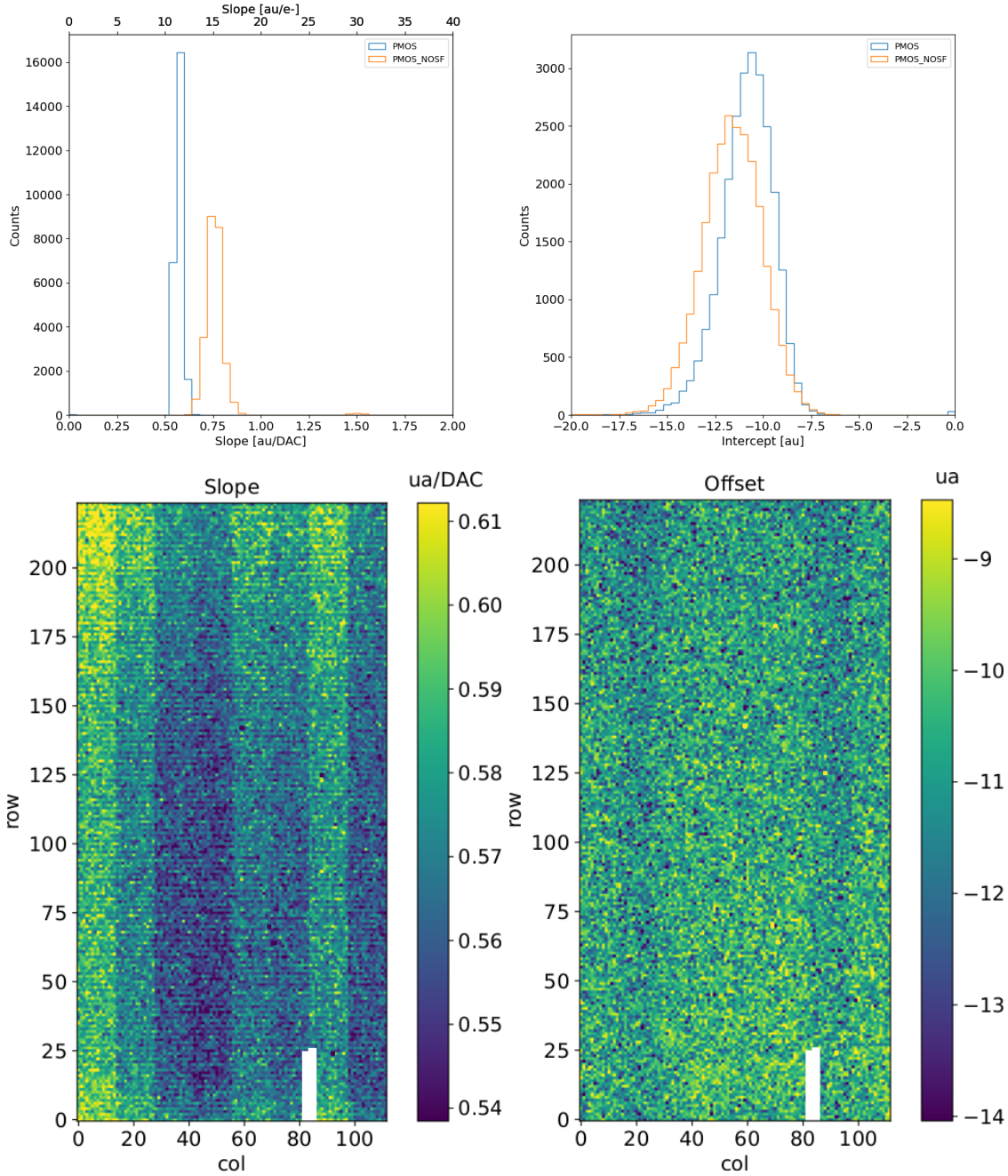


Figure 6.5: Histograms of the calibration parameters, slope (a) and offset (b), found fitting the ToT with a line, for all flavor and with IDB fixed at 40 DAC. Maps of the calibration parameters, slope (a) and offset (b), found fitting the ToT with a line, with IDB fixed at 40 DAC

which does photoelectric effect in the silicon, has an absorption length $\lambda=7 \mu\text{m}$ to $8 \mu\text{m}$, and the probability of being absorbed in the $25 \mu\text{m}$ thick epitaxial layer is ~ 0.95 . The electron emitted has an energy equal to the photon one, so recalling that the mean energy needed to produce a couple electron-vacuum is 3.65 eV , the signal produced by the Fe55 source is expected to be 1616 e- . In figures ?? and ?? are shown two histograms of the ToT spectrum of the Fe55 source for two different pixels. The peak corresponds to the events with completely absorption of the charge produced in the depleted region, while

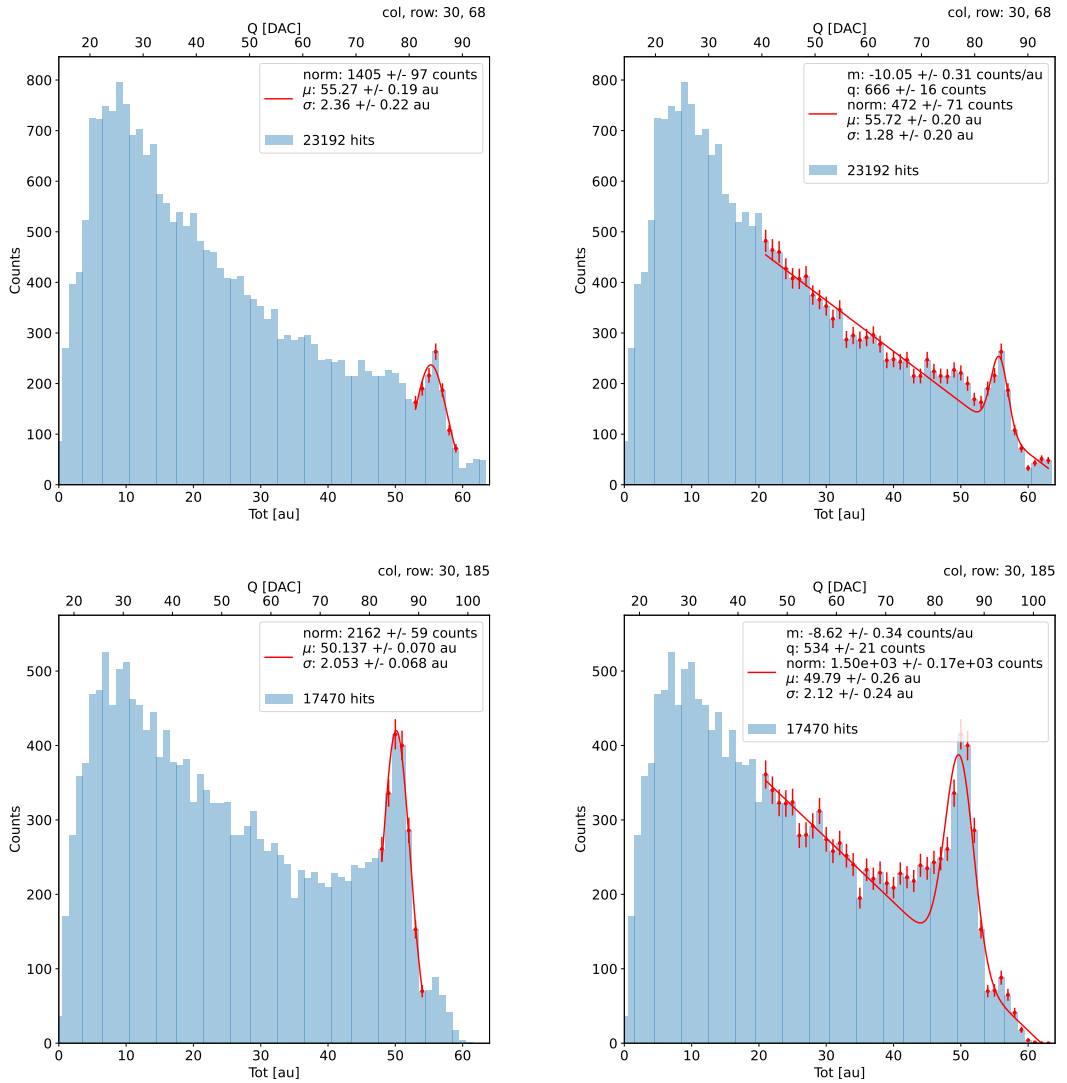


Figure 6.6: due pixel per far vedere la differenza tra i fit. Sottolinea che in rosso ci sono i bin fittati. La doppia scala utilizza le info trovate nel paragrafo precedente per il dato pixel in questione. Per avere una corrispondenza grezza in elettroni basta moltiplicare per 20 e- / dac.

1039 the long tail on the left to all the events with partial absorption due to charge sharing
 1040 among neighbors pixels. In order to reduce the charge sharing, the pixel dimension in
 1041 TJ-Monopix2 has been reduced down to **check**. The events on the right side of the peak,
 1042 instead, corresponds to the K_β photons. Looking at the histograms for pixel (30, 185) and
 1043 (30,69) a significant difference in the peak to tail ratio leaps out. This difference in the
 1044 efficiency of detecting the signal can be related with the position of the pixel in the matrix:
 1045 in particular pixels in the upper part of the matrix (rows 112-224) have a more prominent
 1046 peak, while in pixels in the lower part (rows 0-111) there is a higher partial absorption. I
 1047 recall now that there is a slightly difference in the structure of the low dose-epi layer (??)
 1048 among the rows in the matrix, in particular pixels in rows 112-224 are supposed to have
 1049 a higher efficiency in the pixel corner.

1050 For the calibration I have need to establish the peak position; to do that I perform a

1051 fit of the ToT histogram of each pixels. As fit functions I test both the solutions below:

$$f(x, N, \mu, \sigma) = \frac{N}{\sigma\sqrt{2\pi}} e^{-\frac{1}{2}(\frac{(x-\mu)}{\sigma})^2} \quad (6.7)$$

$$f(x, m, q, N, \mu, \sigma) = m x + q + \frac{N}{\sigma\sqrt{2\pi}} e^{-\frac{1}{2}(\frac{(x-\mu)}{\sigma})^2} \quad (6.8)$$

Nel primo caso ho fissato pochi pixel attorno a picco: il range è stato determinato ..

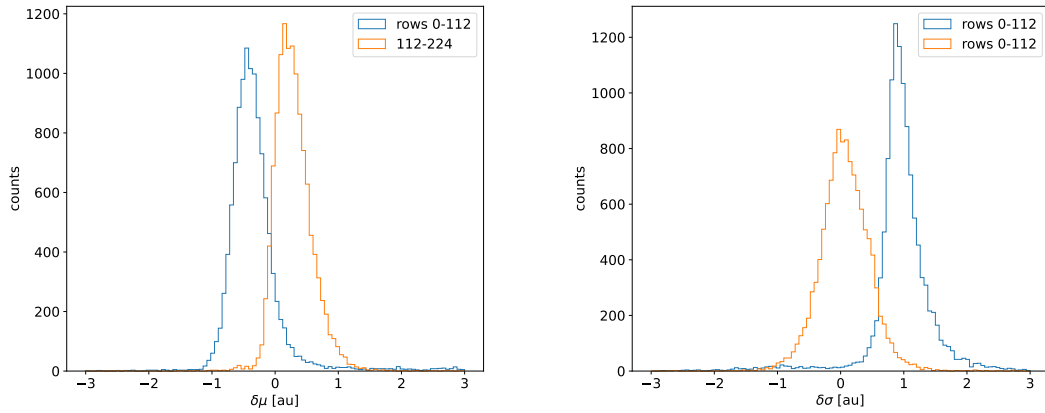


Figure 6.7: Here there are shown the defference between the parameters μ and σ fitted with only a gaussian and with a gaussia plus a line. When $\mu < 0$ the fit function 6.7 has given a worst peak (shifted on the left); when $\sigma < 0$, 6.8 has given a worst peak width (larger sigma)

1052
 1053 **controlla. Nel secondo caso invece il range è.. Controlla sullo script** Even if the difference
 1054 in the peak position between the two cases is not really relevant (6.7) being of the order
 1055 of 0.8-1.5 %, it still introduces a systematic effect moving the peak on the left because of
 1056 the contribution of the tail. Indeed, we know that the sharp edge on the right corresponds
 1057 to the complete absorption of the photon, so excluding the little bump on the right, the
 1058 more the fitted parameter is on the right, the better the fit is. Moreover, there is also
 1059 systematic effect on the peak width, infact the worst fit also gives an overestimation of
 1060 the peak width. Even looking at the χ^2 , the fit function 6.7 seems so be the better choise,
 1061 except for a sample of pixels on the lower part of the matrix, the one with lower efficiency.

1062 Mappa del ferro da cui, come descritto enll'equazione si ricava la capacity. La struttura
 1063 a bande della capacità ha origine nel plot... e quindi nella calibrazione. Andando a vedere
 1064 gli istogrammi di queste due variabili si vedono dei picchi. C'è qualche struttura nella
 1065 matrice che condiziona il funzionamento delle righe? Larghezza della gaussiana: fai il
 1066 discorso a cosa contribuisce ad un picco così largo. è compatibile con quanto ti aspetti?

1067 6.1.4 PMOS flavor: changing the bias

1068 In order to study the behavior of the sensor changing the bias, I perform some injection
 1069 scans in different configurations. The thickness of the depletion has to be considered
 1070 indeed an important parameters for the efficiency of the signal, and in particular it plays
 1071 an important role if bho, trova qualcosa da dire.

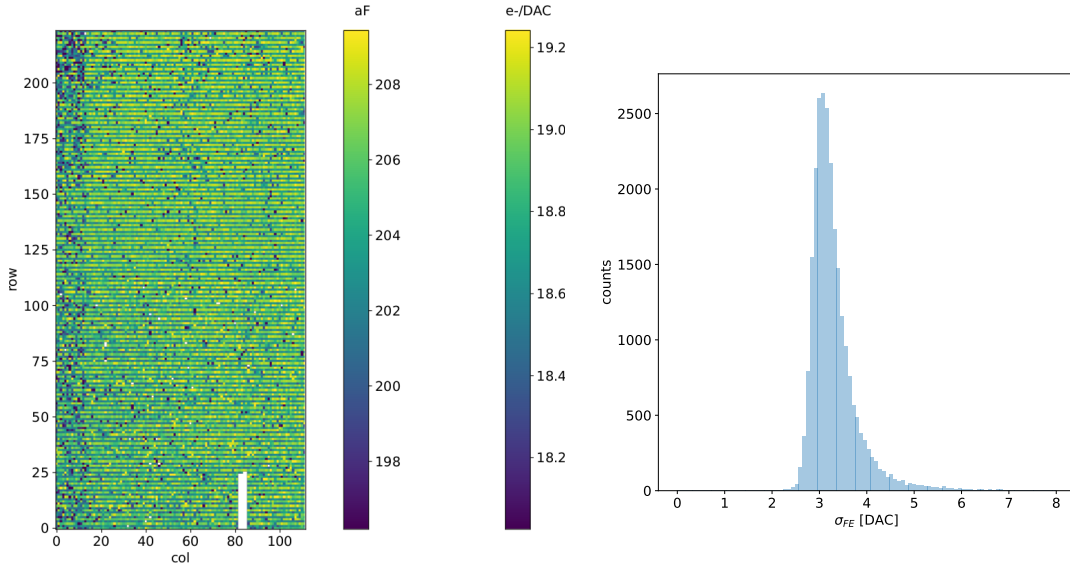


Figure 6.8

	-6 V	-3 V	0 V
Threshold [DAC]	20.04 ± 1.6	21.0 ± 1.6	24.5 ± 1.8
Noise [DAC]	0.613 ± 0.075	0.625 ± 0.078	0.822 ± 0.098
Slope [au/DAC]	0.726 ± 0.027	0.707 ± 0.028	0.573 ± 0.021
Offset [au]	-10.8 ± 1.9	-11.2 ± 1.8	-11.1 ± 1.5

Table 6.3: The errors are the standard deviations of the corresponding distributions.

Given that the chip under examination has a gap in the low dose epi-layer (look at chapter ??) we were not able to change independently the bias of the substrate (PSUB) and of the p-well (PWELL), but they must be kept at the same value, differently from other chips, where they can be changed as reported in figure 4.10. Turning down the bias, the depletion region narrows and the efficiency reduces in particular in the pixel corner; **La soglia si alza di meno di 1/3, mi sarei aspettata un po' di più guardando il plot. Attenzione che il plot non è fatto con un ngap, quindi ci sta che il guadagno lì cali più bruscamente. poi non si capisce benissimo dalla colormap. Anche la slope diminuisce di circa meno di un terzo. Il noise aumenta leggermente. Il picco del ferro invece si sposta a sinistra di un terzo. Lo spostamento è dovuto alla diminuzione del gain, che influenza sul ToT.**

6.1.5 Measurements with radioactive sources

Signal response characterization using radioactive sources and cosmic rays have been made. The Sr90 source emits electrons that: lo spettro ha un cutoff a che E?

conto/plot sulla differenza elettrone sr e mip. The signal generated by electrons is similar to the one generated by minimum ionizing particle (MIPS). The spectrum is expected to follow a Langau-Gauss distribution

- sommato i cluster Spiega la tua definizione di cluster.
- plot dello spettro del ferro convertendo in elettroni per il PMOS flavor e facendo la somma dei cluster.

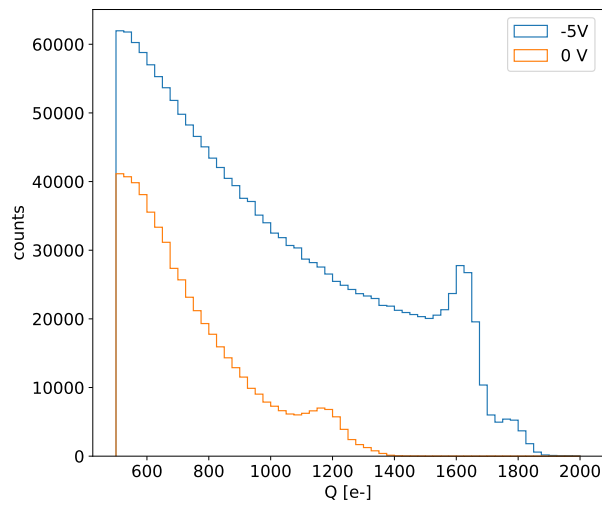


Figure 6.9: With the same acquisition time.

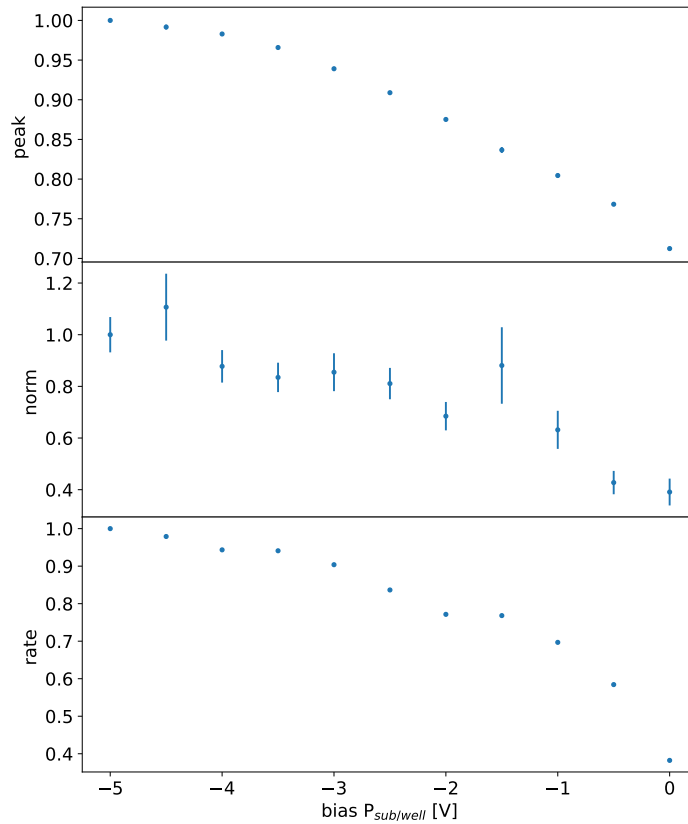


Figure 6.10: da rifare tenendo la sorgente ferma tra un’acquisizione e l’altra

- 1091 • di che la tua definizione di cluster è ok perchè sono quasi tutti vicini: plot con la
 1092 distanza e qualche stima delle coincidenze casuali.
 1093 • mappa di qualche evento di cluster sia per Sr che per FE

- 1094 • istogrammi in carica, con carica sommata di Sr e Fe, oer il flavor PMOS dove hai
 1095 fatto la calibrazione o per tutti?

1096 Spiega che con il flavor HV abbiamo una perdita di sengnale, fai vedere uno spettro di
 1097 delle misure dell 8 marzo.

1098 6.1.6 Dead time measurements

1099 The hit loss is due to analog and digital pile up: the first one occurs when a new hit
 1100 arrives during the pre-amplifier response, the second instead, which is the more relevant
 1101 contribution with high rate, while the information of the previous hit has not yet been
 1102 transferred to the periphery. As only one hit at a time can be stored on the pixel's RAM,
 1103 until the data have completed the path to get out, the pixel is paralyzed and the dead time
 1104 τ almost corresponds with the time needed to trasmit the data-packets off-chip. Since the
 1105 exportation of data from pixel to the EoC occurs via a 21-bits data bus, only one clock
 1106 cycle is need to transfer the data to the end of column and the dead time bottleneck is
 1107 given by the bandwidth of the serializer at the EoC. In our setup the serializer operates
 1108 at 40 MHz, thus to transmit a data packet (27-bit considering the addition at the EoC)
 1109 at least 675 ns are needed. For what we have said so far, the R/O is completely sequential
 1110 and therefore is expected a linear dependence of the reading time on the number of pixels
 1111 to read:

$$\tau = 25 \text{ ns} \times (\alpha N + \beta) \quad (6.9)$$

1112 where α and β are parameters dependent on the readout chain setting.

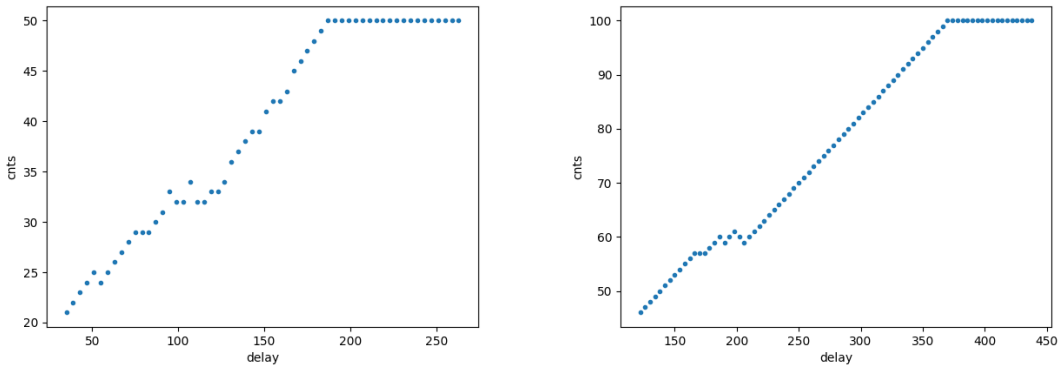
1113 To measure and test the linearity of the reading time with the number of pixels firing,
 1114 I have used the injection mode available on the chip. Indeed, the injection mode allows
 1115 fixing not only the amplitude of the pulse, which corresponds to the charge in DAC units,
 1116 but also the period and the width. I have injected a fix number of pulses (100) and looked
 1117 for the rate when the efficiency decreases. Moreover to test that there is no dependece of
 1118 the digital readout time from the charge of the pulse, I have try to change the amplitude of
 1119 the pulse injected, but the parameters found were consistent with the default configuration
 1120 ones.

1121 *Al posto degli esempi con 5 e 10 pixels metterei un esempio dell'efficienza vs il periodo
 1122 quando leggo un singolo pixel. Una cosa che volevo fare era anche provare a fittare la slope
 1123 con cui l'efficienza scende: se la slope è uguale per tutti il readout diventa completamente
 1124 predittivo.*

1125 While the single pixel reading time and the dead time do not depend on the position
 1126 on the pixel matrix and are equal to 106 (46+60) clock counts within 1 clock count, on
 1127 the other hand the τ depends on the pixel position on the matrix when more than one
 1128 pixel are firing. In particular the priority chain goes from row 224 to row 0, and from col
 1129 0 to 112, that means the last pixels to be read is the one on le bottom right corner of the
 1130 matrix.

1131 In figure 6.13 is reported the reading time versus the number of pixels injected; the
 1132 R/O parameters that control the reading time and their default values are reported on
 1133 table ??.

1134 The factor α , referring to eq. 6.9 is proportional to the difference (STOP_FREEZE
 1135 - START_READ), while the offset β lies between 5 and 15 clock counts. Since through
 1136 the injection a random hit rate on the matrix can't be simulated, as the coordinates



(a) efficiency vs DELAY 5 pixels

(b) efficiency vs DELAY per 10pixels

Parameter	Value [DAC]	Value [μ s]
START_FREEZE	64	1.6
STOP_FREEZE	100	2.5
START_READ	66	1.65
STOP_READ	68	1.7

Table 6.4: Default configuration of the R/O parameters

1137 of the pixels to inject must be specified, for convenience I used the pixels on the same
 1138 column/row. No difference in the α and β coefficients has been observed between the two
 case.

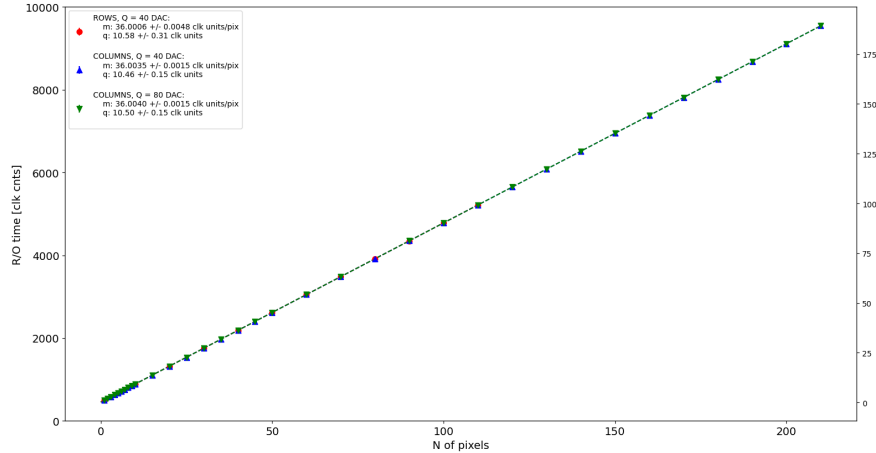


Figure 6.12

1139
 1140 Ci sarebbe da spiegare perchè i parametri che usiamo noi come default non sono quelli
 1141 che minimizzano il tempo di lettura. La spiegazione è che "Abbiamo copiato i valori
 1142 dal repository di quelli di Bonn". Un'altra domanda potrebbe essere: come mai non ho
 1143 esplorato una zona più vasta per i parametri del R/O. Cambiando molto i parametri del
 1144 R/O la lettura non funzionava per niente: ad esempio CONF_STOP_FREEZE non può
 1145 essere impostato nè sopra 105 nè sotto 95

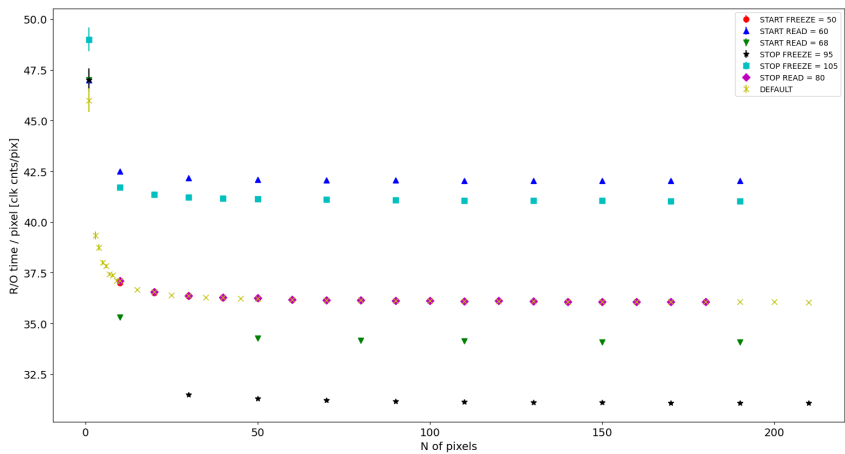


Figure 6.13

1146 6.2 ARCADIA-MD1 characterization

₁₁₄₇ **Chapter 7**

₁₁₄₈ **Test beam measurements**

₁₁₄₉ During August 2022 a testbeam took place in Santa Chiara hospital in Pisa, where a
₁₁₅₀ new accelerator designed for both medical research and R&D in FLASH-RT, and for this
₁₁₅₁ reason called "ElectronFlash", have been installed a few months ago.

₁₁₅₂ The motivation of the testbeam measurements were testing TJ-Mopopix1 in condition
₁₁₅₃ different from the one foreseen during the design and also testing the mechanical and the
₁₁₅₄ DAQ setup for other future measurement. TJ-Monopix1 is supposed to be employed for
₁₁₅₅ tracking in HEP experiments while our goal was testing the possibility of integrating the
₁₁₅₆ charge released by more particles at ultra high hit rate achievable with the accelerator.
₁₁₅₇ **Una frase di disclaimer sul fatto che non siamo riusciti a testare quello che volevamo.**

₁₁₅₈ In medical physics the dose is indeed the standard parameter to characterize the beam
₁₁₅₉ because of its obvious relation with the damage caused in the patient: firstly the oncolo-
₁₁₆₀ gists prescribe a certain dose taking into account the efficacy of the treatment and then
₁₁₆₁ the medical physicists, on the basis of simulations, decide the energy and the intensity of
₁₁₆₂ the beams to dispense the prescribed dose amount. By the point of view of the instrumen-
₁₁₆₃ tation and the testing on it, a more common and useful parameter is instead the rate or
₁₁₆₄ the fluence of particles. The conversion between the two quantity can be found thinking to
₁₁₆₅ the definition of dose: it is the concentration of energy deposited in tissue as a result of an
₁₁₆₆ exposure to ionizing radiation. Assuming total absorption of electrons in water, defined
₁₁₆₇ by law as the ordinary reference medium, the dose can be expressed as:

$$D[Gy] = \frac{NE[eV]}{\rho[g/cm^3]A[cm^2]x[cm]} \quad (7.1)$$

₁₁₆₈ After having applied the conversion of the energy from eV to J and noticed that $E/\rho x$
₁₁₆₉ roughly corresponds to the stopping power S of electrons in water, a simple estimation of
₁₁₇₀ the dose released in water is:

$$D[Gy] = 1.602 \cdot 10^{-10} N[cm^{-2}] S[MeVcm^2/g] \quad (7.2)$$

₁₁₇₁ **7.1 Apparatus description**

₁₁₇₂ The accelerator is placed in a bunker inside the hospital: to shield the outdoor from
₁₁₇₃ ionizing radiation the bunker has very thick walls of cementum and both the control units
₁₁₇₄ of the accelerator and of the detector were placed outside the bunker. For practicability
₁₁₇₅ reasons the power supply were the only device to be placed inside the bunker.

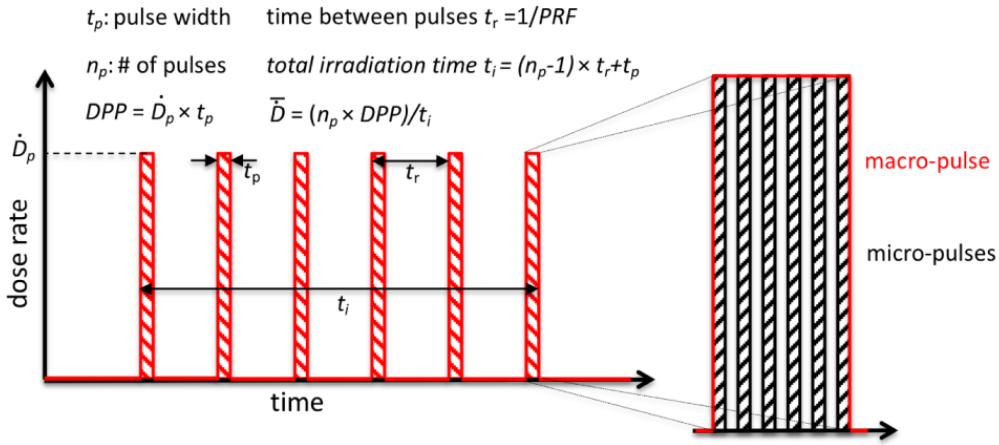


Figure 7.1: Typical beam structure of a beam with the standard characteristic quantity

\bar{D}	Dose rate (mean dose rate for a multi-pulse delivery)	0.005-10000 Gy/s
\dot{D}	Intra pulse dose rate (dose rate in a single pulse)	0.01-1 10^6 Gy/s
DDP	Dose in a single pulse	0.04-40 Gy
PRF	Pulse repetition frequency (number of pulses delivered per unit of time)	1-350 Hz
t_p	Pulse width	0.2-4 μ s
n	Number of pulses	single/pulse train

Table 7.1: The parameters that can actually be set by the control unit are the PRF, DDP, t_p and n (in particular singular irradiation or pulse train), while the other changes consequently.

1176 7.1.1 Accelerator

1177 The ElectronFlash accelerator is an electron Linear Accelerator (LINAC) with two energy
 1178 configurations, at 7 MeV and 9 MeV, and it can reach ultra high intensity (40 Gy/pulse)
 1179 keeping the possibility of accessing many different beam parameters and changing them
 1180 independently from each other. This characteristic is fundamental for research in FLASH-
 1181 RT, both for the medical aspects and for the studies on detectors; for example is not really
 1182 clear the dependence of the efficacy of the FLASH effect on the whole dose parameters.
 1183 ElectronFlash is **almost the only one** in the world having this characteristic, **ricontrolla sulla**
 1184 **review, c'era qualcosa che puoi dire.** The accelerator implements a standard beam struc-
 1185 ture for RT with electrons (fig. 7.1), that is a macro pulse divided in many micropulses;
 1186 the parameters used to set the dose and their range of values settable by the control unit
 1187 is reported in table 7.1.

1188 The accelerator is provided of a set of triod cannons ~ 1.2 m long and with diameters
 1189 from 1 cm to 12 cm and a collimator that can be used as beam shaper to produce a
 1190 squircle shape. The triode, which is made by plexiglass, must be fix to the gun during the
 1191 irradiation and is needed for producing an uniform dose profile (fig.7.2) which is desired
 1192 for medical purpose via the scattering of electrons with the plexiglass.

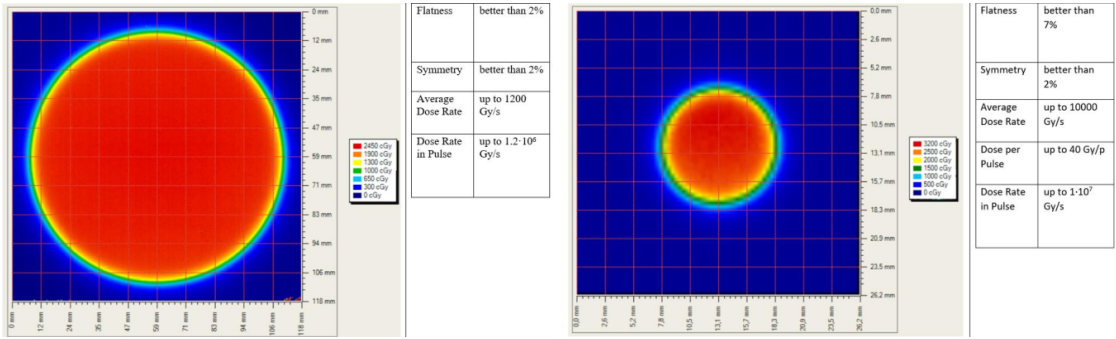


Figure 7.2: Two example of x-y isodose curves for two different triodes, 10 cm and 1 cm respectively, reported by the producer in the manual with the specific of the accelerator (S.I.T. - Sordina IORT Technologies S.p.A.). With the smaller collimator the dose rate in pulse is comparatively higher.

1193 7.1.2 Mechanical carriers

1194 The tested detector consists in one chip, the Device Under Test (DUT), mounted on a
 1195 board and connected to FPGA with same arrangement of figure 7.7. These have been
 1196 positioned vertically in front of the triode on a table specifically built for the testbeam.
 1197 The tree board have been enclosed in a box of alluminium with a window on the DUT
 1198 and with the required holes at the side to enable the biasing via cables and the connection
 1199 with the DAQ provided via ethernet cable. A trigger signal coming from the control unity
 1200 and syncronize with the pulses emitted from the beam has been also sent to the FPGA.
 1201 This signal cannot be considered a trigger signal, since being a prototypes TJ-Monopix1
 1202 has been designed to be triggerless, but the time of arrival of this signal, which is saved
 1203 by the FPGA, can allow the reconstruction of the of the arrival of the bunch during the
 1204 analysis.

1205 In order to shield the sensor from the whole particles emitted from the gun, two
 1206 alluminium collimators have been fabricated: one has been positioned at the triode exit
 1207 while the other in front of the DUT. The collimators are $t=32$ mm thick and have a
 1208 diameter d equal to 1 mm: assuming a beam divergence bigger than $d/t=1/32 = 1.8^\circ$,
 1209 which is the case, the collimator at the triode output was supposed to work as a point
 1210 source and to reduce the rate on the DUT of a factor at least $4 \cdot 10^{-4}$. The second one,
 1211 being near the DUT, was instead supposed to shield the sensor from the electrons which
 1212 have passed the first one, except for a region of 1 mm^2 configurable using **come si chiamano**
 1213 **quei cacciavitini per settare la posizione?**.

1214 7.2 Measurements

1215 Because of the dead time of TJ-Monopix1 it is not possible resolving the bunch sub-
 1216 structure and almost no one pixel can read more than a hit per bunch. I recall, indeed,
 1217 that the dead time per pixel depends on the location on the priority chain for the readout
 1218 and for each pixel $\lesssim 1 \mu\text{s}$ (fig. 7.7) are needed; therefore only a few pixels at the top of
 1219 the priority chain (at the upper left of the matrix) can fire a second time, since they in
 1220 principle can be read the first time before the end of the pulse (assuming a pulse duration
 1221 in $2 \mu\text{s}-4 \mu\text{s}$) and then can be hit again.

1222 Since resolving the single electron track is impossible, a way this sensor could be used

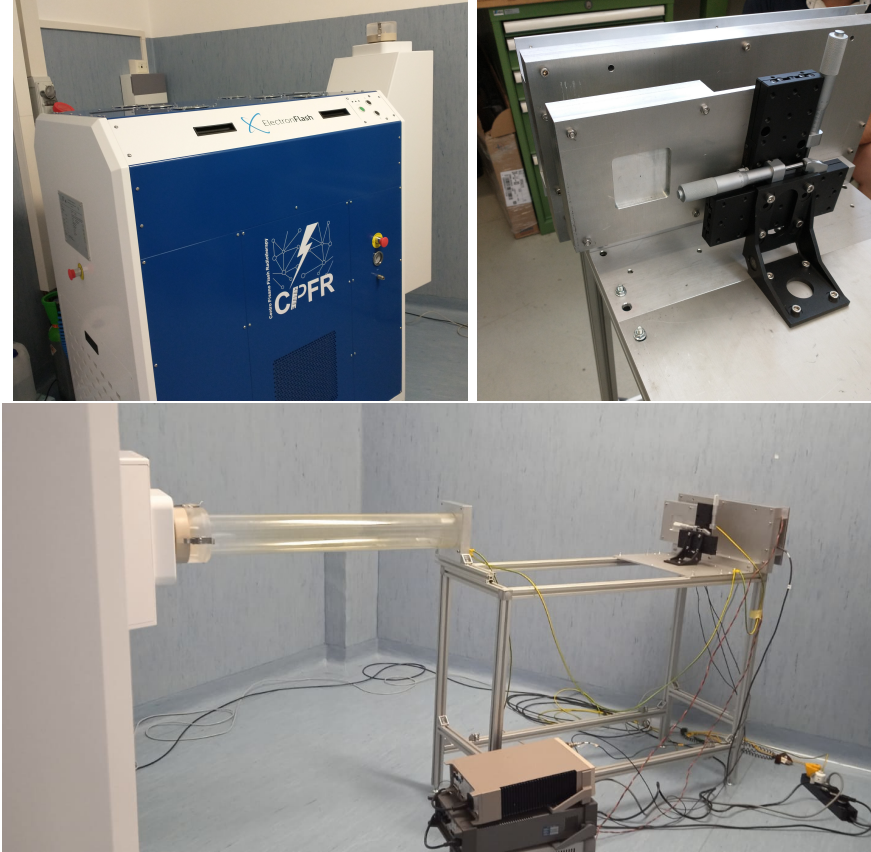


Figure 7.3: Experimental set up. (a) Electron flash accelerator: gantry rotante che consente un orientamento del fascio da 0° 90° (orizzontale / verticale) in tempo reale monitorato da un inclinometro integrato. the gun can be rotated from 90° to 0° (vertical/orizontal). (b) Collimator and DUT box. (c) Whole structure: we used the 10 cm diameter and 1.2 m long triode; the DUT which is in the box behind the two collimators is connected to the power supply units.

in such context is reducing its efficiency and taking advantage of the analog pile up and of the linearity of the analog output (ToT), in order to see a signal produced not by the single particle but by more electrons. Reducing the efficiency and the sensibility of the sensor is essential in order to decrease the high charge signal produced in the epitaxial layer: if the sensor is completely depleted the collection efficiency is closer to 1% and if the whole charges produced by a MIP, $80 \text{ e}^-/\mu\text{m}$ about, are collected, the saturation limit is soon reach. Then a condition where there is a partial recombination of the center electron-hole created in the bulk is desiderable. On the other hand, the smaller the output signal value and the higher the rate the detector can cope with: indeed, the rollover constitutes a limit for the usage of the analog output. With the standard configuration of the FE parameters and the epitaxial layer completely depleted, a MIP produces a ToT out of range of representation of 6-bit; so as to obtain smaller output signals one can operate on the reduction of the gain of the preamplifier or on the pulse velocity of returnig to the baseline. Recalling the results in section 6.1.4, I have shown that concerning the PMOS flavor 1, reducing the bias from -6 V to 0 V brings a reduction of efficiency down to 40 %, and a reduction in the gain of a factor $\sim 1/3$, while the reduction of the gain of the preamplifier allows a reduction of **circa 10, ma da controllare**.

1240 In order to taking advantage of the analog pile up and integrating the charge, for
 1241 semplicity assume of two electrons, the second one must hit the pixel before the ToT goes
 1242 under the threshold. The general condition is then $\overline{\Delta T} < \overline{ToT}$, but if a high $P_\mu(n \geq 1)$ is
 1243 required, a lower $\overline{\Delta T}$ may be desired:

$$P(n \geq 1) = \sum_{n=1}^{\infty} \frac{e^{-\mu} \mu^n}{n!} = 1 - P(0) = 1 - e^{-\mu} \quad (7.3)$$

1244

$$\mu = \frac{\overline{ToT}}{\overline{\Delta T}} \quad (7.4)$$

1245 If a $P_\mu(n \geq 1) = 99\%$ then the $\overline{\Delta T}$ must be $\sim 0.22 \overline{ToT}$. The ToT is in range [0,64] but
 1246 since the rollover must be avoided, the \overline{ToT} must be lower than 32, and then the minimum
 1247 rate on the pixel must be 1.25 MHz.

1248

1249 During the testbeam many runs have been performed, spanning the energy, the dose
 1250 per pulse and the four possible configurations with/without the collimators. We have used
 1251 the PMOS flavor 1 in the standard configuration: we have biased the PWELL and PSUB
 1252 at -6 V and set the standard default FE parameters reported in table ???. During all the
 1253 acquisitions we have used pulses with t_p of 4 μm and with the smallest PRF settable, which
 1254 is 1 Hz, in order to start in the most conservative working point exluding the digital pile
 1255 up of events from different bunch: even if the whole matrix turns on and there are 25000
 1256 hits, the total readout time corresponding to 25 ms is still lower than the time between two
 1257 consecutive pulses. The readout starts with the trailing edge of the first pulse going down
 1258 the threshold, ~ 50 clk = 1.25 μs after this moment the FREEZE signal is sent to the whole
 1259 matrix, and the trasmittion of the data to the EoC begins. The hits read are the ones
 1260 whose TE occurred during the 50 clk counts; the ones, instead, whose TE occur during the
 1261 FREEZE are stored in the pixel memory and read during a second readout. Obviously
 1262 since the readout of the fist sub-pulse finishes much later than the bunch ends up, each
 1263 pixel can be store only one hit. An example of the two sub-pulses is shown in figure ???:
 1264 in the acquisition we injected 5 pulses with both the collimators mounted on the table.
 1265 Looking at the spectrum **si vede che lo spettro del secondo pulse ha una coda più lunga a
 1266 destra: questo è dovuto al fatto che le hit con tot lungo hanno il TE che cade durante il
 1267 FREEZE e quindi vengono lette durante il secondo impulso.** On the other hand the 2D
 1268 histograms, being uniform and not showing disomogenities, suggest that the collimators
 1269 do not shield all the particles: this was due to a photon background higher than expected.
 1270 When we have put aside the collimators, instead, the fluence was too high that **the whole
 1271 matrix turns on in 50 clk counts; then the 2 pulses substructure no more appears (fig. 7.6).**
 1272 **CONTROLLA PERCHÈ PORTEBBE ESSERE UNA CAZZATA**

1273 After the testbeam a simulation of the emission of electrons from the accelerator and
 1274 their path across the triode and the collimators has been developed via Geant-4 **come si
 1275 ringrazia il lavoro di qualcuno in maniera formale?**. The high background we saw although
 1276 the collimators were mainly produced by electrons Bremsstrahlung during the transition
 1277 through the alluminium collimators. **dalla simulazione si è visto che nessun elettrone
 1278 arriva sul chip quando ci sono montati i collimatori, mentre nel caso senza collimatori gli
 1279 eventi sono sostanzialmente tutti elettroni (frazione di fotoni prodotti in aria è?).** The
 1280 photons' simulated spectrum in the three configurations are shown in figure ???. **confronto
 1281 con quello che vedo nello spettro sopra: dati.**

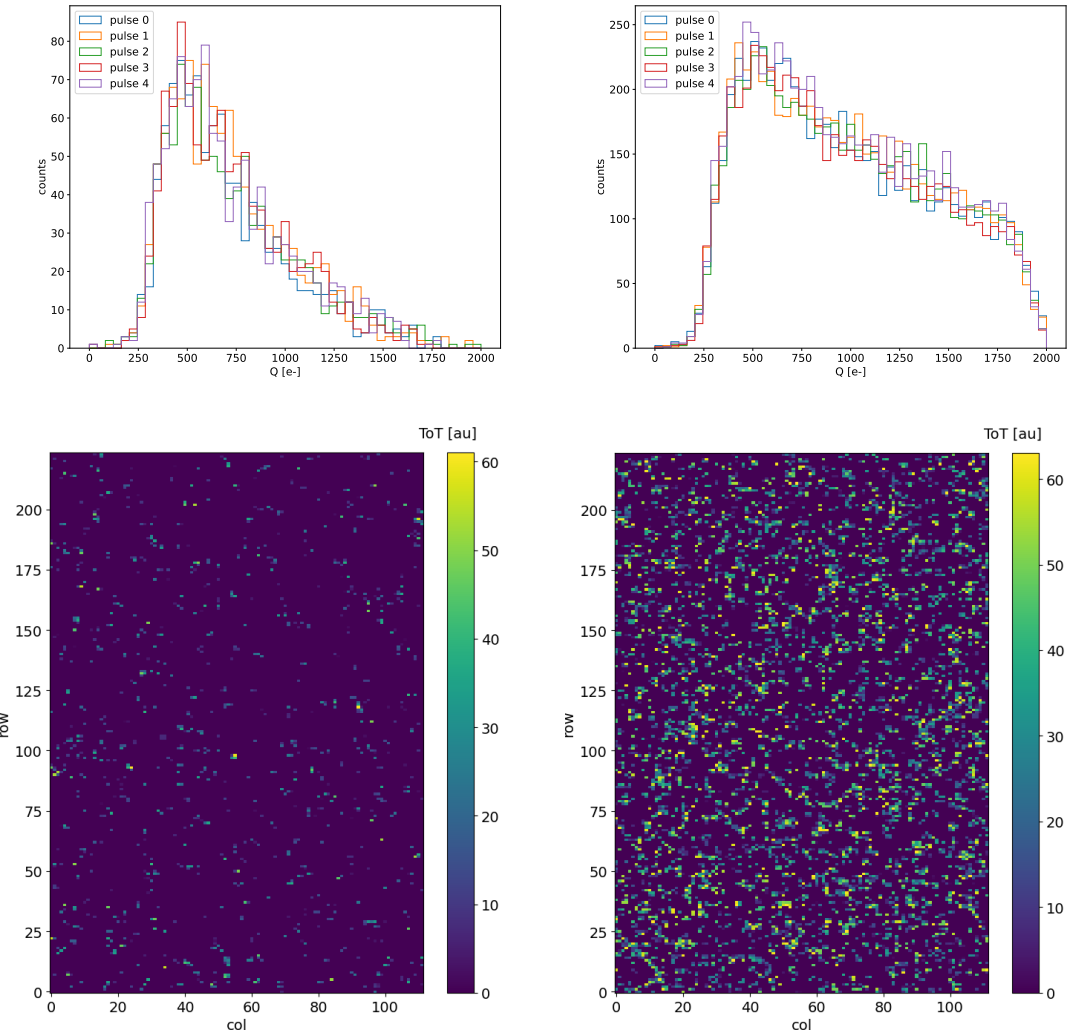


Figure 7.4: Acquisition with both the collimators: 5 pulses at $DDP=0.07$ Gy. (a) Spectrum of the charge released in the sensor: to apply the conversion I used the information found in the previous chapter. (b) 2D histogram of the ToT of the hits arrived in the sub-pulses.

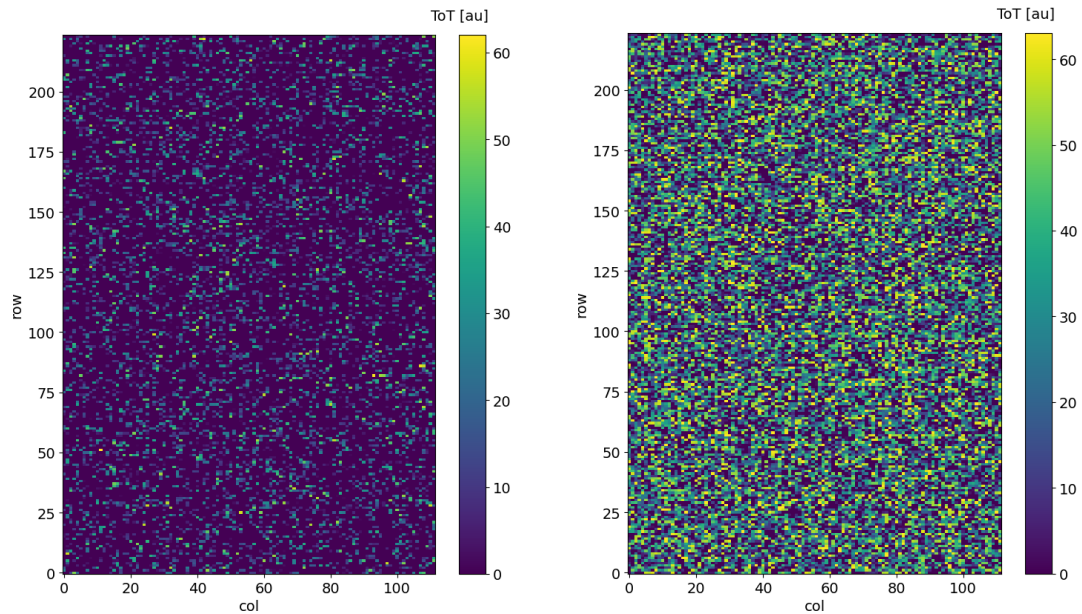


Figure 7.5: Acquisition with both the collimators: 5 pulses at DDP=0.6 Gy. 2D histogram of the ToT of the hits arrived in the sub-pulses. Compared with the previous maps, since the DDP is much higher, more pixels turn on.

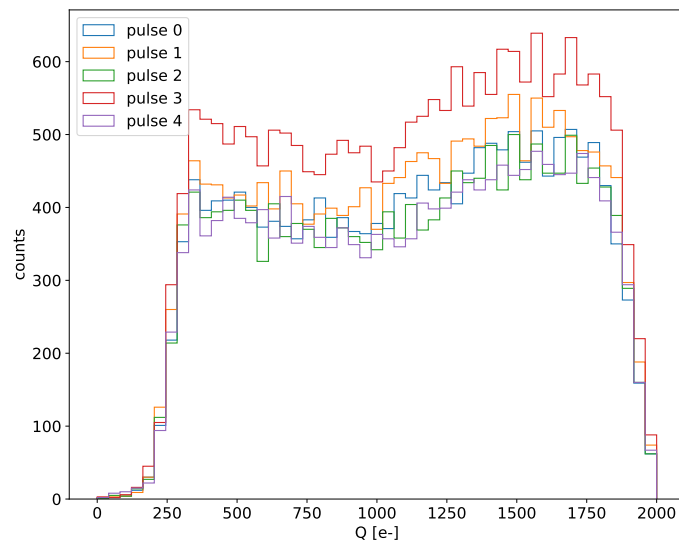


Figure 7.6: Acquisition without any collimator: 5 pulses at DDP=0.04 Gy.

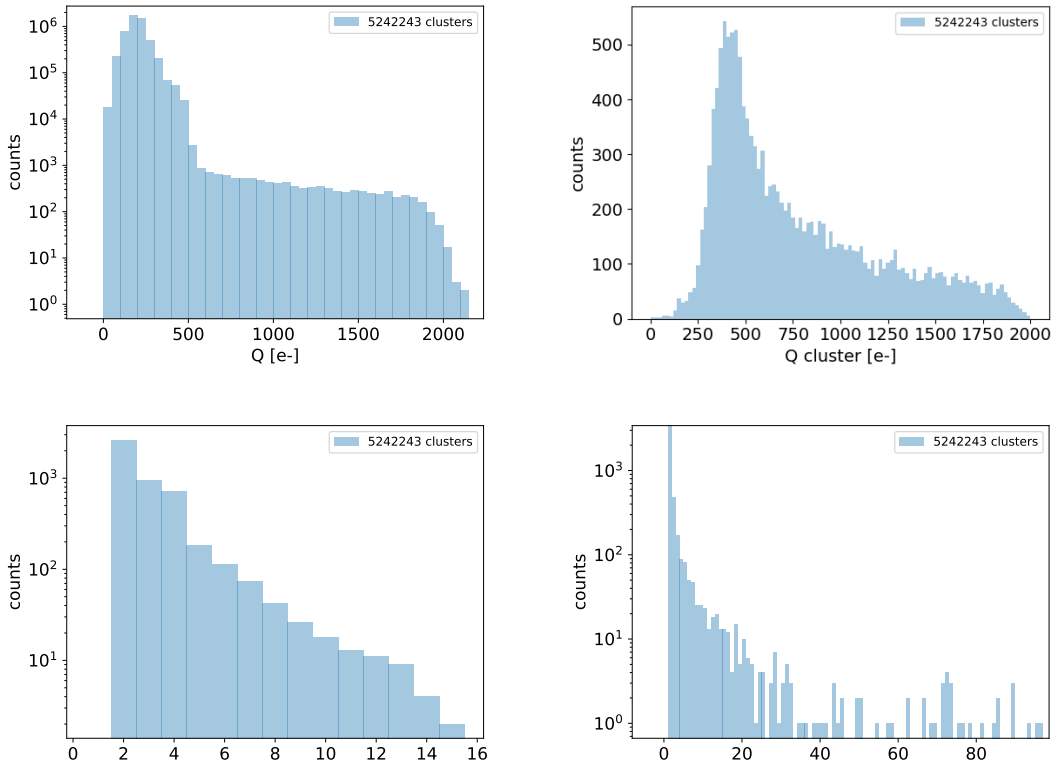


Figure 7.7: plot dei raggi cosmici da rigenerare

- 1282 • plot n di eventi che vedo con le diverse configurazioni
- 1283 • simulazione surya
- 1284 • confronta con misure dello spettro che vediamo senza e con collimatori.

1285 7.2.1 MIP spectrum using cosmic rays as source

1286 Since a MIP should produce about 2 ke- in the epitaxial layer, it should provide a signal
 1287 that in our conditions (full depletion and high gain) rolls over: in this situation making
 1288 prediction on the spectrum expected for MIPs becomes hard. Therefore, in order to
 1289 compare the spectrum observed at the testbeam with one certainly produced by MIP I
 1290 have made some acquisitions without any radioactive source, in order to look at the cosmic
 1291 ray events. To be confident with having selected MIPs from cosmic rays and cut the noise, I
 1292 have selected only the events with multiple hits: these events are mainly clusters produced
 1293 by the same impinging particle since the random coincidence probability is very low. In
 1294 fact the cosmic rays and noise rates on the whole matrix are respectively 0.02 Hz and
 1295 $\sim\text{Hz}$, the dead time in such a low occupancy condition can be always approximated with
 1296 $1\text{ }\mu\text{m}$ (this is not completely true for multiple hits events for which the priority chain
 1297 should be considered), the random coincidence rate is 10^{-8} Hz . Come mai lo spettro in
 1298 lab è diverso da quello visto con gli elettroni da 9 MeV al santa chiara? Chiedi a Surya il
 1299 rate visto sul detector senza collimatori.

1300 **Appendix A**

1301 **Pixels detector: a brief overview**

1302 **A.1 Radiation damages**

1303 Radiation hardness is a fundamental requirement for pixels detector especially in HEP
1304 since they are almost always installed near the interaction point where there is a high
1305 energy level of radiation. At LHC the ϕ_{eq} per year in the innermost pixel detector is
1306 $10^{14} n_{eq}/cm^2$; this number reduces by an order passing to the outer tracker layer [2] pag
1307 341 Wermes. Here the high fluence of particles can cause a damage both in the substrate
1308 of the detector and in the superficial electronics.

1309 The first one has a principal non ionizing nature, due to a non ionizing energy loss
1310 (NIEL), but it is related with the dislocation of the lattice caused by the collision with
1311 nuclei; by this fact the NIEL hypothesis states that the substrate damage is normalized to
1312 the damage caused by 1 MeV neutrons. Differently, surface damages are principally due
1313 to ionizing energy loss.

1314 **DUE PAROLE IN PIÙ SUL SURFACE DAMAGE** A charge accumulation in oxide
1315 (SiO_2) can cause the generation of parasitic current with an obvious increase of the 1/f
1316 noise. Surface damages are mostly less relevant than the previous one, since with the de-
1317 velopment of microelectronics and with the miniaturization of components (in electronic
1318 industry 6-7 nm transistors are already used, while for MAPS the dimensions of compo-
1319 nents is around 180 nm) the quantity of oxide in circuit is reduced.

1320 Let's spend instead two more other words on the more-relevant substrate damages:
1321 the general result of high radiation level is the creation of new energy levels within the
1322 silicon band gap and depending on their energy-location their effect can be different, as
1323 described in the Shockley-Read-Hall (SRH) statistical model. The three main consequence
1324 of radiation damages are the changing of the effect doping concentration, the leakage
1325 current and the increasing of trapping probability.

1326 **Changing of the effective doping concentration:** is associated with the cre-
1327 ation/removal of donors and acceptors center which trap respectively electrons/holes from
1328 the conduction band and cause a change in effective space charge density. Even an in-
1329 version (p-type becomes n-type¹) can happen: indeed it is quite common at not too high
1330 fluences ($\phi_{eq} 10^{12-13} n_{eq} cm^{-2}$). A changing in the doping concentration requires an adjust-
1331 ment of the biasing of the sensor during its lifetime (eq.2.2) and sometimes can be difficult
1332 keeping to fully deplete the bulk.

1333 **Leakage current:** is associated with the generation-recombination centers. It has

¹L'INVERSIONE OPPOSTA NON CE L'HAI PERCHÈ?

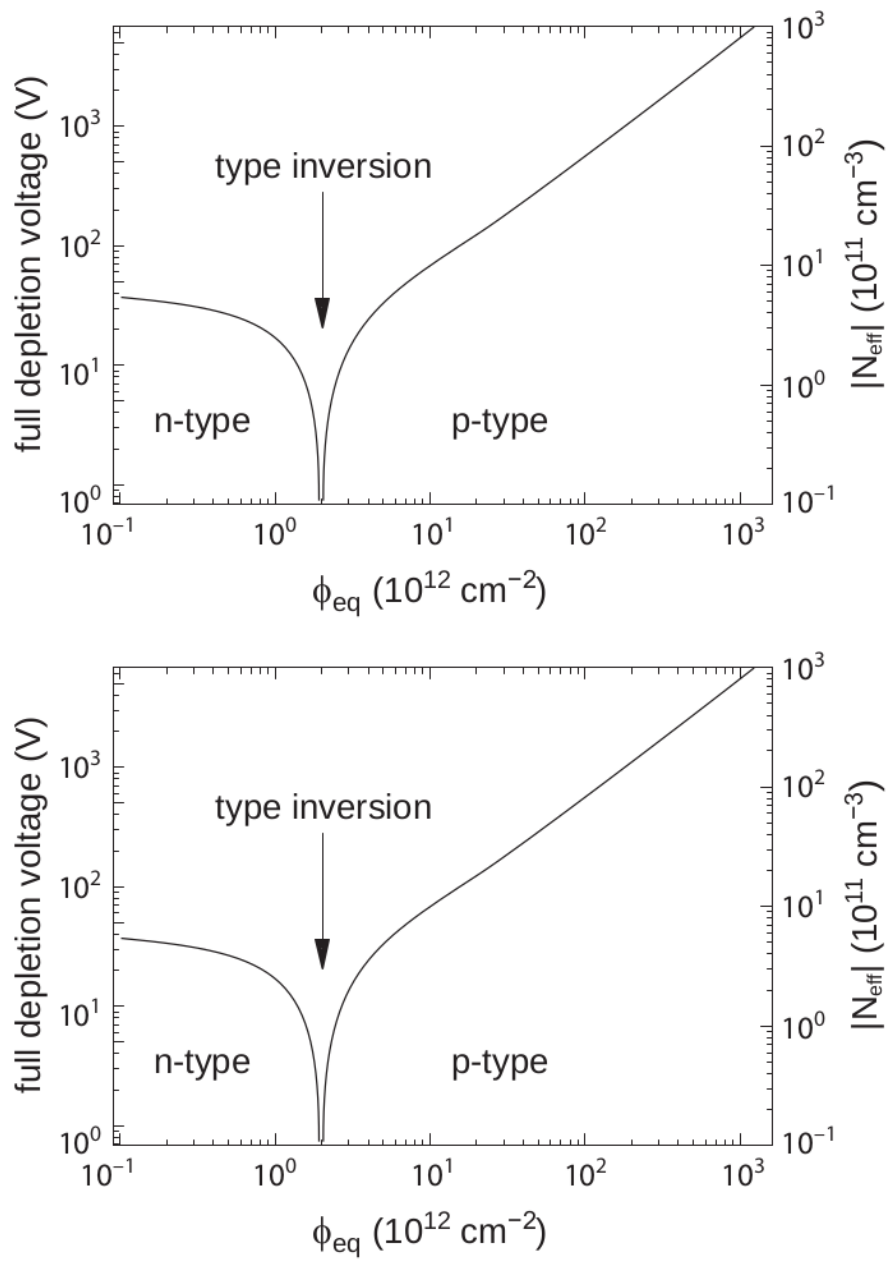


Figure A.1: 1b

1334 a strong dependence with the temperature ($I_{leak} \propto T^2$), whose solution is therefore to
1335 operate at lower temperature.

1336 **Increase of trapping probability:** since the trapping probability is constant in the
1337 depleted region, the collected charge decreases exponentially with the drift path. The
1338 exponential coefficient, that is the mean trapping path, decreases after irradiation and
1339 typical values are 125-250 μm and must be compared with the thickness of the depleted
1340 region which () corresponds to the mean drift path.

1341 Different choices for substrate resistivity, for junctions type and for detector design are
1342 typically made to fight radiation issues. Some material with high oxygen concentration
1343 (as crystal produced using Czochralki (Cz) or float-zone (Fz) process (**CONTROLLA**
1344 **LA DIFFERENZA TRA I DUE**)) for example, show a compensation effect for radiation
1345 damage; another example is the usage of n+ -in-p/n sensors (even if p+ -in-n sensors are
1346 easier and cheaper to obtain) to get advantage of inversion/to have not the inversion (since
1347 they are already p-type). After inversion the n+p boundary, coming from n+ in-n, but to
1348 keep using the sensor the depletion zone still must be placed near the diode.

1349 Single Event Upset, in sostanza è quando un bit ti cambia valore (da 0 a 1 o viceversa)
1350 perché una particella deposita carica nell'elettronica che fa da memoria registro/RAM/....
1351 Questo tipo di elettronica ha bisogno di un sacco di carica prima che il bit si "fippi"
1352 (cambi valore), infatti tipicamente per avere un SEU non basta una MIP che attraversa
1353 esattamente quel pezzo di chip in cui è implementata la memoria, ma un adrone che faccia
1354 interazione nucleare producendo più carica di quanto farebbe una MIP. Questo metodo pur
1355 essendo più comodo richiede less amount of area ha però come drawback che il registro può
1356 essere soggetto a SEU problema non trascurabile in acceleratori come HL-LHC adronici

Bibliography

- [1] W. Snoeys et al. “A process modification for CMOS monolithic active pixel sensors for enhanced depletion, timing performance and radiation tolerance”. In: (2017). DOI: <https://doi.org/10.1016/j.nima.2017.07.046>.
- [2] H. Kolanoski and N. Wermes. *Particle Detectors: Fundamentals and Applications*. OXFORD University Press, 2020. ISBN: 9780198520115.
- [3] E. Mandelli. “Digital Column Readout Architecture for the ATLAS Pixel 0.25 um Front End IC”. In: (2002).
- [4] M. Garcia-Sciveres and N. Wermes. “A review of advances in pixel detectors for experiments with high rate and radiation”. In: (2018). DOI: <https://doi.org/10.1088/1361-6633/aab064>.
- [5] C. Marinas. “The Belle-II DEPFET pixel detector: A step forward in vertexing in the superKEKB flavour factory”. In: (2011). DOI: [doi:10.1016/j.nima.2010.12.116](https://doi.org/10.1016/j.nima.2010.12.116).
- [6] J. Baudot. “First Test Results Of MIMOSA-26, A Fast CMOS Sensor With Integrated Zero Suppression And Digitized Output”. In: (2010). DOI: [doi:10.1109/NSSMIC.2009.5402399](https://doi.org/10.1109/NSSMIC.2009.5402399).
- [7] A. Dorokhov. “High resistivity CMOS pixel sensors and their application to the STAR PXL detector”. In: (2011). DOI: [doi:10.1016/j.nima.2010.12.112](https://doi.org/10.1016/j.nima.2010.12.112).
- [8] Giacomo Contin. “The STAR MAPS-based PiXeL detector”. In: (2018). DOI: <https://doi.org/10.1016/j.nima.2018.03.003>.
- [9] Nolan Esplen. “Physics and biology of ultrahigh dose-rate (FLASH) radiotherapy: a topical review”. In: (2020). DOI: <https://doi.org/10.1088/1361-6560/abaa28>.
- [10] M. Dyndal et al. “Mini-MALTA: Radiation hard pixel designs for small-electrode monolithic CMOS sensors for the High Luminosity LHC”. In: (2019). DOI: <https://doi.org/10.1088/1748-0221/15/02/p02005>.
- [11] M. Barbero. “Radiation hard DMAPS pixel sensors in 150 nm CMOS technology for operation at LHC”. In: (2020). DOI: <https://doi.org/10.1088/1748-0221/15/05/p05013>.
- [12] K. Moustakas et al. “CMOS Monolithic Pixel Sensors based on the Column-Drain Architecture for the HL-LHC Upgrade”. In: (2018). DOI: <https://doi.org/10.1016/j.nima.2018.09.100>.
- [13] I. Caicedo et al. “The Monopix chips: depleted monolithic active pixel sensors with a column-drain read-out architecture for the ATLAS Inner Tracker upgrade”. In: (2019). DOI: <https://doi.org/10.1088/1748-0221/14/06/C06006>.

- 1391 [14] D. Kim et al. “Front end optimization for the monolithic active pixel sensor of the
1392 ALICE Inner Tracking System upgrade”. In: *JINST* (2016). DOI: doi:10.1088/
1393 1748-0221/11/02/C02042.
- 1394 [15] L. Pancheri et al. “A 110 nm CMOS process for fully-depleted pixel sensors”. In:
1395 (2019). DOI: <https://doi.org/10.1088/1748-0221/14/06/c06016>.
- 1396 [16] L. Pancheri et al. “Fully Depleted MAPS in 110-nm CMOS Process With 100–300-
1397 um Active Substrate”. In: (2020). DOI: 10.1109/TED.2020.2985639.